



# Using Species A Rotavirus Reverse Genetics to Engineer Chimeric Viruses Expressing SARS-CoV-2 Spike Epitopes

Ola Diebold,<sup>a</sup> Victoria Gonzalez,<sup>a</sup> Luca Venditti,<sup>b</sup> Colin Sharp,<sup>a</sup> Rosemary A. Blake,<sup>a</sup> Wenfang S. Tan,<sup>a</sup> Joanne Stevens,<sup>a</sup> Sarah Caddy,<sup>c</sup>  Paul Digard,<sup>a</sup> Alexander Borodavka,<sup>b</sup>  Eleanor Gaunt<sup>a</sup>

<sup>a</sup>Infection and Immunity Division, Roslin Institute, University of Edinburgh, Easter Bush Campus, Midlothian, United Kingdom

<sup>b</sup>Department of Biochemistry, University of Cambridge, Cambridge, United Kingdom

<sup>c</sup>Cambridge Institute of Therapeutic Immunology and Infectious Disease, Department of Medicine, University of Cambridge, Cambridge, United Kingdom

**ABSTRACT** Species A rotavirus (RVA) vaccines based on live attenuated viruses are used worldwide in humans. The recent establishment of a reverse genetics system for rotaviruses (RVs) has opened the possibility of engineering chimeric viruses expressing heterologous peptides from other viral or microbial species in order to develop polyvalent vaccines. We tested the feasibility of this concept by two approaches. First, we inserted short SARS-CoV-2 spike peptides into the hypervariable region of the simian RV SA11 strain viral protein (VP) 4. Second, we fused the receptor binding domain (RBD) of the SARS-CoV-2 spike protein, or the shorter receptor binding motif (RBM) nested within the RBD, to the C terminus of nonstructural protein (NSP) 3 of the bovine RV RF strain, with or without an intervening *Thosea asigna virus 2A (T2A)* peptide. Mutating the hypervariable region of SA11 VP4 impeded viral replication, and for these mutants, no cross-reactivity with spike antibodies was detected. To rescue NSP3 mutants, we established a plasmid-based reverse genetics system for the bovine RV RF strain. Except for the RBD mutant that demonstrated a rescue defect, all NSP3 mutants delivered endpoint infectivity titers and exhibited replication kinetics comparable to that of the wild-type virus. In ELISAs, cell lysates of an NSP3 mutant expressing the RBD peptide showed cross-reactivity with a SARS-CoV-2 RBD antibody. 3D bovine gut enteroids were susceptible to infection by all NSP3 mutants, but cross-reactivity with SARS-CoV-2 RBD antibody was only detected for the RBM mutant. The tolerance of large SARS-CoV-2 peptide insertions at the C terminus of NSP3 in the presence of T2A element highlights the potential of this approach for the development of vaccine vectors targeting multiple enteric pathogens simultaneously.

**IMPORTANCE** We explored the use of rotaviruses (RVs) to express heterologous peptides, using SARS-CoV-2 as an example. Small SARS-CoV-2 peptide insertions (<34 amino acids) into the hypervariable region of the viral protein 4 (VP4) of RV SA11 strain resulted in reduced viral titer and replication, demonstrating a limited tolerance for peptide insertions at this site. To test the RV RF strain for its tolerance for peptide insertions, we constructed a reverse genetics system. NSP3 was C-terminally tagged with SARS-CoV-2 spike peptides of up to 193 amino acids in length. With a T2A-separated 193 amino acid tag on NSP3, there was no significant effect on the viral rescue efficiency, endpoint titer, and replication kinetics. Tagged NSP3 elicited cross-reactivity with SARS-CoV-2 spike antibodies in ELISA. We highlight the potential for development of RV vaccine vectors targeting multiple enteric pathogens simultaneously.

**KEYWORDS** rotavirus, NSP3, VP4, reverse genetics

Species A rotaviruses (RVAs) are a leading cause of severe acute gastroenteritis in infants and young children worldwide, accounting for ~128,500 deaths annually (1–3). Likewise, rotavirus (RV)-associated enteritis in young calves and piglets has a

**Editor** Tom Gallagher, Loyola University Chicago

**Copyright** © 2022 American Society for Microbiology. All Rights Reserved.

Address correspondence to Eleanor Gaunt, Elly.Gaunt@ed.ac.uk, or Alexander Borodavka, ab2677@cam.ac.uk.

The authors declare no conflict of interest.

**Received** 22 March 2022

**Accepted** 31 May 2022

**Published** 27 June 2022

significant economic impact on livestock production as a result of the high morbidity and mortality caused (4–7). Two human live attenuated RV vaccines, Rotarix and RotaTeq, have proven effective in reducing the incidence of RV-related hospitalization and mortality internationally (2, 8–10). Vaccination strategies for livestock rely on induction of active or passive immunity using animal RV vaccines (11–14).

RVA is a double-stranded RNA (dsRNA) virus with 11 genome segments encoding six structural viral proteins (VP1–VP4, VP6, and VP7) and depending on the strain, 5 or 6 nonstructural proteins (NSP1–NSP5 ± NSP6) (3, 15, 16). The mature infectious virion, termed a triple-layered particle (TLP), consists of an outer layer formed by VP4 and VP7. A double-layered particle (DLP), nested within the TLP, contains the intermediate and inner layers of the capsid formed by VP6 and VP2 respectively (3). RV primarily infects mature enterocytes of the intestinal epithelium and replicates exclusively in the cytoplasm (17, 18). Efficient RV cell entry requires proteolytic cleavage of the outer capsid protein VP4 into VP8\* (28 kDa) and VP5\* (60 kDa) domains by trypsin-like proteases of the host gastrointestinal tract (19–22). The VP8\* lectin domain mediates RV attachment to different host cell receptors such as sialic acid-containing glycans, histo-blood group antigens, and integrins, depending on the virus strain (18, 23–25). Following endocytosis, low calcium levels in endosomes trigger the dissociation of VP7 and VP4, releasing the transcriptionally active DLP into the cytoplasm (3). Here, DLPs transcribe capped, nonpolyadenylated, positive-sense single-stranded RNA transcripts, which act as templates for viral protein translation (3). The 11 mRNAs share a conserved terminal 3'-UGUGACC sequence that contains *cis*-acting signals important for transcription by the RNA-dependent RNA polymerase (VP1) (26–30). The 3'-GACC sequence is bound by the N terminal of NSP3, while the C terminus of NSP3 interacts with the eukaryotic protein initiation factor 4G1 (eIF4G1) (31–33). NSP3 displaces poly-A binding protein from ribosomal complexes to favor the translation of viral over host cell proteins (34–37).

The molecular characterization of RVs has historically proven challenging due to inefficiencies of the helper virus-dependent reverse genetics systems available for controlled mutagenesis studies (38–41). Recently, however, Kanai et al. (42) developed a plasmid only-based reverse genetics system for the simian RV strain SA11. The plasmid-only reverse genetics system has been optimized to study the functions of RV proteins, to generate RV reassortants and RV reporter expression systems, and conceptualize novel vaccine platforms (43–45). Using the plasmid only-based reverse genetics system, recombinant RVs harboring chimeric VP4 proteins that showed efficient replication in cell culture and neutralizing activity in mice have also been engineered (46–48). Protection from infection with RV is primarily mediated by heterotypic neutralizing antibodies that target VP4 and/or VP7 (47, 49). VP4 is therefore highly immunogenic and an important target for adaptive immunity (49, 50). Thus, the potential for VP4 to express heterologous epitopes from different RV strains may provide a delivery platform for expression of different vaccine antigens, although peptide insertions into VP4 has not previously been tested. Additionally, the plasmid only-based reverse genetics system has been utilized to generate a repertoire of recombinant RVs expressing fluorescent reporter proteins (48, 51). The C terminus of the SA11 NSP3 open reading frame (ORF) was fused to a porcine teschovirus translational 2A element followed by various reporters including UnaG, mKate, mRuby, or TagBFP to successfully yield two uncoupled proteins without compromising virus replication (51). A more recent study showed that the C terminus of SA11 NSP3 can express different peptides of the severe acute respiratory syndrome coronavirus 2 (SARS-CoV-2) spike protein with minimal impact on endpoint titers (52). This has highlighted the potential to use RVs as expression vectors for development of polyvalent vaccines for enteric viruses.

In response to the recent emergence of SARS-CoV-2, the causative agent of coronavirus disease 2019 (COVID-19), several platforms have been utilized for vast global vaccine production (53, 54). Current licensed vaccines include examples that employ mRNA (Pfizer-BioNTech, Moderna) or viral vectors (AstraZeneca, Janssen) to deliver genetic material encoding the SARS-CoV-2 spike protein in order to stimulate the

production of neutralizing antibodies and T-cell-mediated immune responses that target this protein (55–58). High neutralizing antibody titers are strongly associated with specificity for the receptor binding domain (RBD) of the spike protein, making it the most immunogenic antigen (59–62). To assess the potential for generating chimeric vaccines using RV, we used SARS-CoV-2 as a timely and important example, introducing spike peptides into the RV genetic backbone and determining whether chimeric viruses showed cross-reactivity with spike antibodies. For this, the hypervariable region of SA11 VP4 (VP8\* lectin domain) and the C terminus of the bovine RV RF strain NSP3 were modified to express SARS-CoV-2 spike epitopes.

We found that mutating the hypervariable region of SA11 VP4 reduced RV infectivity and mutants expressing spike peptides did not cross-react with SARS-CoV-2 spike antibodies, suggesting limitations of VP4 tagging as a strategy for live attenuated vaccine development. Using our newly established plasmid-only-based reverse genetics system for the bovine RV RF strain, we rescued infectious viruses expressing either the RBD or the RBM of the SARS-CoV-2 spike protein, with similar titers and replication kinetics to those of the wild-type (WT) virus. These viruses cross-reacted with RBD antibodies in enzyme-linked immunosorbent assay (ELISA) and were able to infect bovine gut enteroids, inferring the potential of the system for use in live attenuated vaccine development.

## RESULTS

***In vitro* synthesis of RV proteins tagged with SARS-COV-2 spike peptides.** We engineered a panel of SA11 strain VP4 plasmids with SARS-CoV-2 spike peptide sequences inserted into the hypervariable region, and a panel of RF strain NSP3 plasmids with 3' tags of SARS-CoV-2 RBM or RBD with or without a separating *Thoesa asigna* virus 2A (T2A) peptide (Fig. 1A). VP4 comprises two major domains, VP5\* and VP8\*, which undergo conformational change upon tryptic cleavage that enhances viral entry (20, 63–65). For peptide insertion into VP4, the hypervariable region (residues L164 to N198) within the VP8\* lectin domain was targeted due to the genome plasticity of this region and its virion surface expression (57, 63, 64). The insertion site has been mapped onto the crystal structure of VP4 (Fig. 1B).

To confirm the expression of the spike epitopes by the mutated VP4 and NSP3 segments, coupled *in vitro* transcription and translation (IVT) reactions were carried out using rabbit reticulocyte lysate system supplemented with [<sup>35</sup>S]methionine (Fig. 1B and C).

Following sodium dodecyl sulfate-polyacrylamide gel electrophoresis (SDS-PAGE) and autoradiography, SA11 WT and mutated VP4 constructs produced polypeptide products of the expected protein size throughout (Fig. 1C). The WT RF NSP3 construct expressed a protein of expected size (Fig. 1D, lane 2). RF NSP3 segment incorporating the RBM motif produced a protein of a higher molecular weight consistent with its predicted size (Fig. 1D, lane 3). The T2A\_RBM construct generated a product containing the NSP3 protein that ran slightly higher than WT NSP3 due to the residual C-terminal fusion of partial T2A sequence (66) (Fig. 1D, lane 4, red asterisk). The small size (~10 kDa) of the unconjugated RBM peptide made it difficult to visualize due to comigration with the dye front. Unseparated NSP3-T2A\_RBM, seen as a minor product, was probably produced as a result of unsuccessful ribosome skipping at the T2A site (66) (Fig. 1D, lane 4, black asterisk). As expected, translation of NSP3 fused to the RBD peptide also produced a protein of a higher molecular weight than the WT (Fig. 1D, lane 5). For the T2A\_RBD construct, untagged NSP3 was readily identifiable, and again a fainter band corresponding to the predicted molecular weight of fused NSP3-T2A\_RBD was also seen (Fig. 1D, lane 6, red and black asterisks, respectively). The RBD product (~23 kDa) was reproducibly not detectable, possibly due to discontinued translation as a result of ribosome fall-off at the T2A site, or degradation in the rabbit reticulocyte lysate system. These results show that the spike epitopes were successfully translated in a cell-free system and that the T2A peptide was functional.

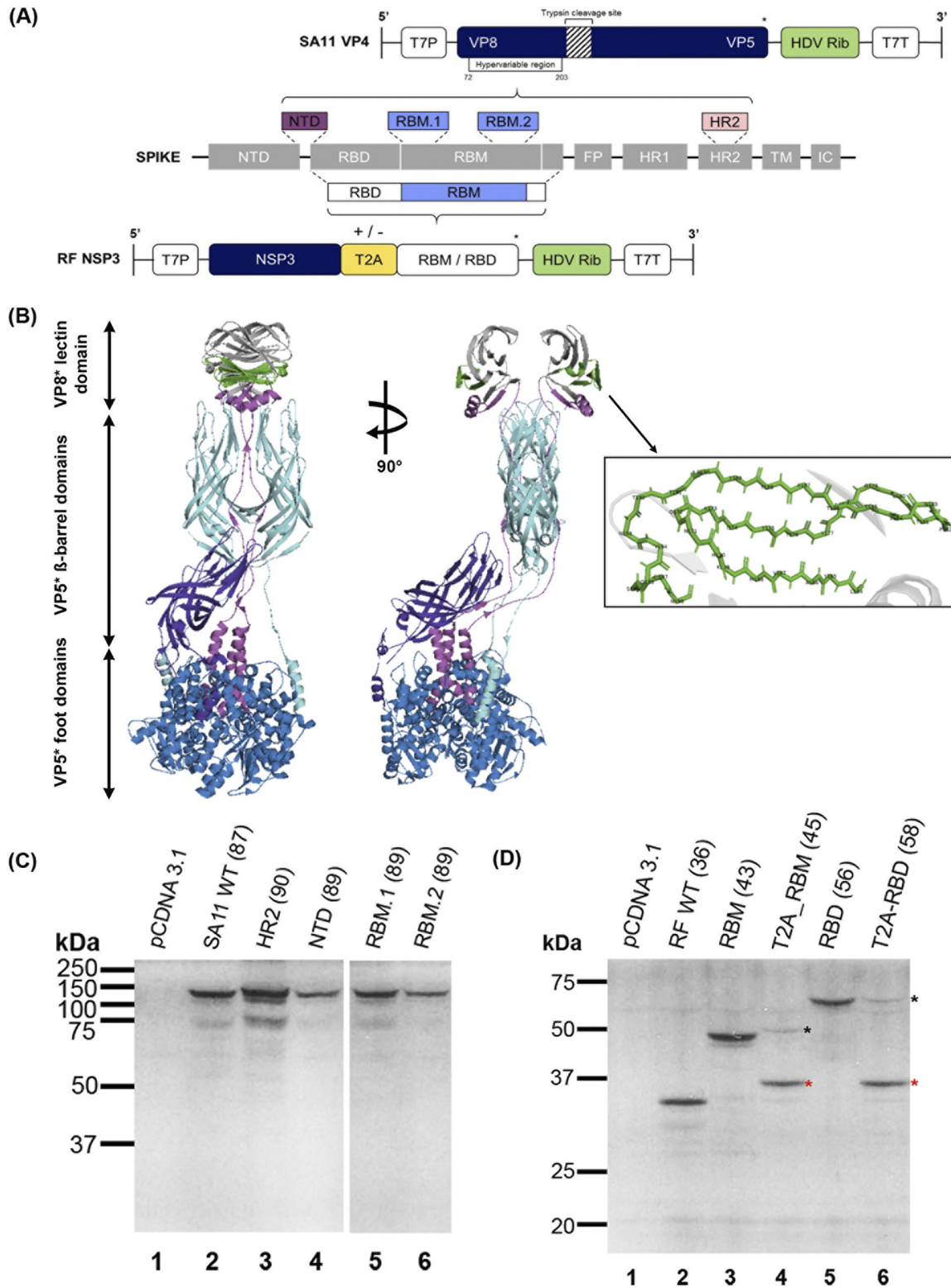


**FIG 1** Design and validation of rotavirus (RV) VP4 and nonstructural protein 3 (NSP3) plasmid constructs used to generate mutant viruses. (A) Schematic showing overall topology of SARS-CoV-2 spike protein in gray boxes: N-terminal domain (NTD), receptor binding domain (RBD), which contains the receptor binding motif (RBM), fusion peptide (FP), heptad repeats 1 and 2 (HR1 and HR2), transmembrane region (TM), and the intracellular domain (IC) (adapted from Lan et al. [62]). Dashed lines represent selected regions of the spike protein (colored boxes) that were inserted into the hypervariable region of the SA11 viral protein 4 (VP4) gene (top) and the C terminus of the RF NSP3 gene (bottom). SA11 VP4 was edited to incorporate either NTD, RBM.1, RBM.2, or HR2 spike peptide sequences. RF NSP3 was fused with either the RBD or RBM sequence with or without *Thosea asigna* virus 2A (T2A) (yellow box), (Continued on next page)

**Establishment of a reverse genetics system for bovine RV RF strain and rescue of mutant viruses.** To develop a reverse genetics system for the bovine RF strain of RV, BSR-T7 cells were transfected with plasmids encoding each of the 11 gene segments of the RF strain along with plasmids encoding the vaccinia virus capping enzyme (D1R and D12L) (Fig. 2A). Transfected cells were cocultured with MA104 cells and supernatant was then passaged on fresh MA104 cells. Following amplification in MA104 cells, supernatant was harvested as virus stock (Fig. 2B). To compare the replication kinetics of the engineered RF virus with the RF isolate, we first performed multi-cycle infections in MA104 cells at a low multiplicities of infection (MOI) (Fig. 2B). The two viruses showed similar overall kinetics, exhibiting exponential growth for around 16 h and then plateauing (Fig. 2B). From 24 hours postinfection (hpi), the titers of rescued RF were approximately a  $\log_{10}$  lower than the RF isolate (24 and 48 hpi: \*,  $P \leq 0.05$ ; 32 hpi: \*\*\*,  $P \leq 0.001$ ) (Fig. 2B). Although the RF isolate replicated better than the engineered RF, the endpoint titer of engineered RF showed that it grows efficiently in cultured cells. These data suggest that the bovine RV RF strain was successfully rescued using a plasmid only-based reverse genetics system.

Next, we used our established reverse genetics system for the bovine RV RF strain to generate the VP4 and NSP3 mutant viruses. With the exception of the N-terminal domain (NTD) mutant, all VP4 mutants displayed significantly lower titers compared to the WT, with an approximately two- $\log_{10}$  decrease in the titers observed across the panel (Fig. 2C). Nonetheless, all VP4 mutants were successfully rescued on all attempts. The VP4 mutants exhibited a similar but smaller speckled plaque phenotype to the WT (Fig. 2D). Statistical analyses of plaque sizes were not performed due to the ambiguities in determining the peripheries of individual plaques and their nonuniform diameters within a well.

In contrast, compared to the WT virus, there were no statistically significant differences observed in titers of any of the NSP3 mutants (Fig. 2E). However, out of three attempts, RBM was successfully rescued twice while T2A\_RBM was rescued at all times, with one of the rescues showing a two- $\log_{10}$  lower titer (Fig. 2E). The RBD mutant was only rescued once with a titer that was a  $\log_{10}$  lower than the WT (Fig. 2E). Although T2A\_RBD rescued on all attempts, it delivered a five- $\log_{10}$  variation in titers between the rescues (Fig. 2E). The viruses with NSP3 tags displayed smaller plaques than the WT, except T2A\_RBM, whose plaques had a similar morphology to that of WT (Fig. 2F). Notably, in the presence of T2A peptide, plaque sizes were larger than when RBM or RBD was fused directly to the C terminus of NSP3 without T2A (Fig. 2F).

Thus, small peptide insertions into the hypervariable region of SA11 VP4 significantly reduced the virus titer, while the efficiency of viral rescue was affected by the size of the peptides fused to the C terminus of RF NSP3. Furthermore, these data demonstrated that the RF strain of RV was successfully rescued from cloned cDNAs (confirmed by sequencing, data not shown).

**Characteristics of VP4 and NSP3 mutant viruses.** Following virus rescue, we first examined the effects of peptide insertion on RV replication in cell culture. Multistep growth curves were performed for the VP4 and NSP3 mutants after infection of MA104 cells at a low MOI. From 24 hpi, all VP4 mutants had significantly lower titers ( $\geq 1\text{-}\log_{10}$ ) than the WT virus for at least one time point during the infection (Fig. 3A). Next, we assessed the impact of the introduced mutations on the total RNA expression levels for

#### FIG 1 Legend (Continued)

represented by +/- sign. Both gene segments were flanked by the T7 promoter (T7P) and the antigenomic hepatitis delta virus (HDV) ribozyme ("HDV Rib," green boxes) followed by T7 terminator (T7T). \*Stop codons. Schematic not to scale. (B) Ribbon representation of VP4 (adapted from Settembre et al. [63]). Two orthogonal views are shown. The VP8\* fragment is in magenta extending into the VP5\* foot domains (in blue), the hypervariable region of VP4 is in gray and the region where SARS-CoV-2 peptides (omitted for clarity) were inserted is in green. VP5\*  $\beta$ -barrel domains are in cyan and purple. (C and D) Coupled in vitro transcription and translation reactions of mutated SA11 VP4 (C) and RF NSP3 (D) segments were carried out using the TnT rabbit reticulocyte lysate system supplemented with [ $^{35}$ S]methionine. Samples were analyzed using SDS-PAGE and autoradiography. The molecular weight marker and the expected product sizes of each segment (in brackets) are indicated (kDa). Empty pCDNA 3.1 vector was used as a negative control. In panel D, black asterisks indicate T2A read-through product and red asterisks identify separated products. WT, wild type.

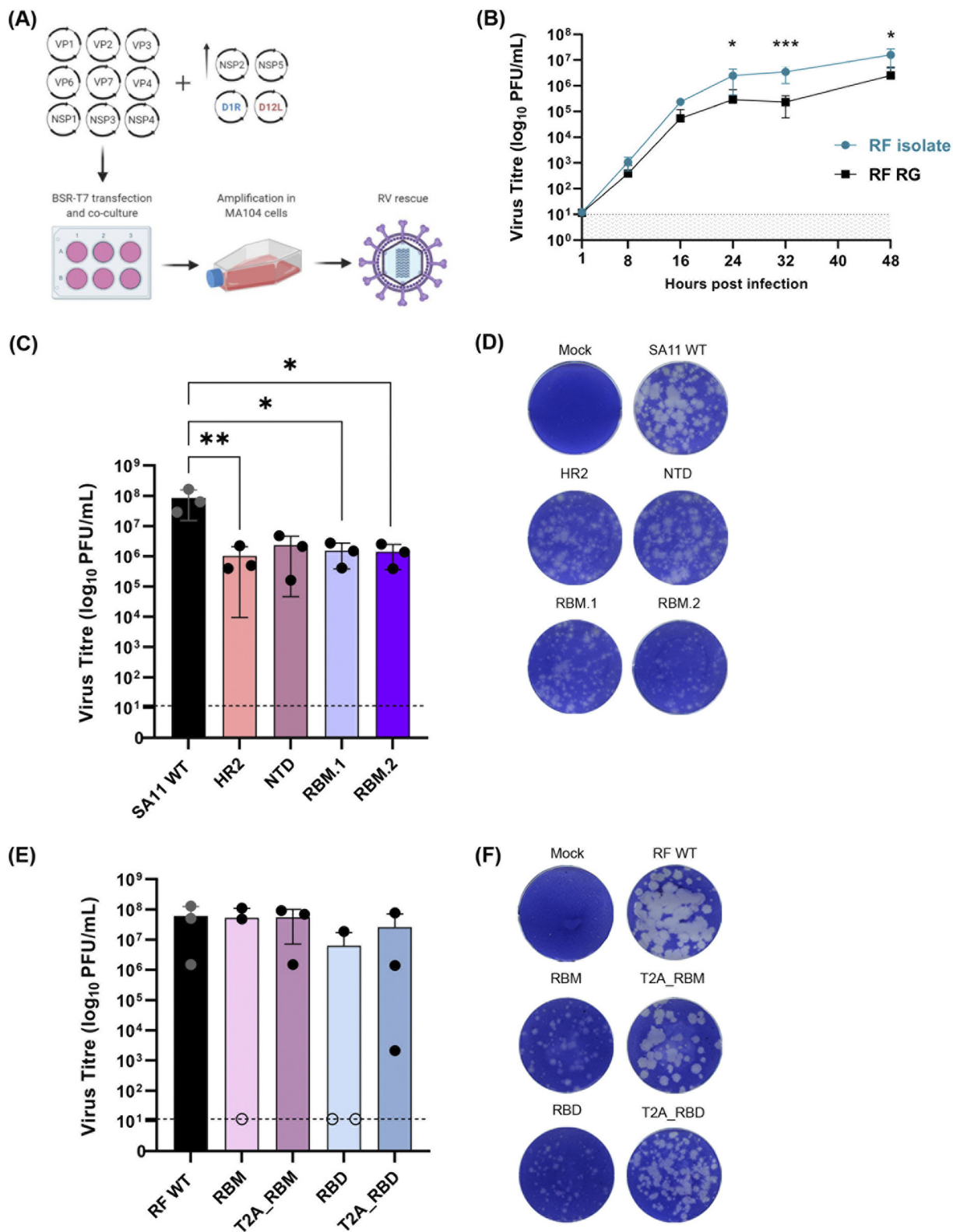


**FIG 2** Generation of VP4 and NSP3 mutant viruses using plasmid-only based reverse genetics system. (A) Schematic representation of a 13-plasmid system for generation of mutant viruses expressing spike epitopes (adapted from Kanai et al. [42] and Komoto et al. [43]; created with BioRender.com). Full-length cDNAs representing each of the 11 gene segments were transfected into BSR-T7 cells with increasing amounts of two plasmids carrying NSP2 and NSP5 genes, along with two plasmids expressing vaccinia virus capping enzyme genes (D1R and D12L). Mutant viruses were rescued following amplification in MA104 cells. (B) Multistep growth curves comparing the bovine rotavirus (RV) RF isolate with reverse genetics (RG) virus. \*,  $P \leq 0.05$  (24 hours postinfection [hpi],  $P = 0.0473$ ; 48 hpi,  $P = 0.0407$ ). \*\*\*,  $P \leq 0.001$  (32 hpi, (Continued on next page)

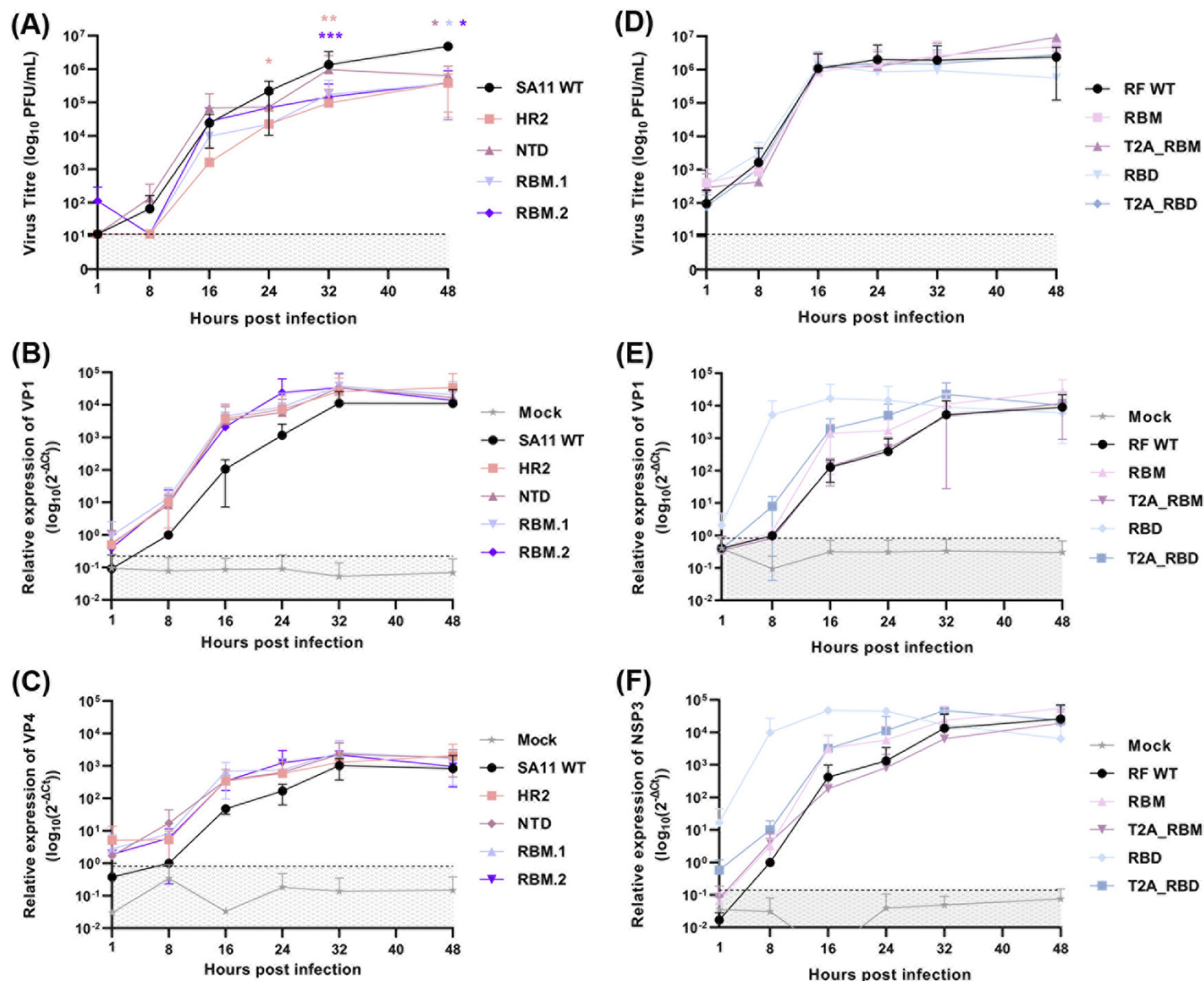


**FIG 3** Replication kinetics and viral RNA content of WT and mutant viruses. (A and B) Multistep growth curves for VP4 and NSP3 mutant viruses respectively. \*,  $P \leq 0.05$  (24 hpi HR2,  $P = 0.041$ ; 48 hpi NTD,  $P = 0.047$ ; RBM.1,  $P = 0.045$ ; RBM.2,  $P = 0.031$ ). \*\*,  $P \leq 0.01$  (32 hpi HR2,  $P = 0.009$ ). \*\*\*,  $P \leq 0.001$  (32 hpi RBM.2,  $P = 0.0006$ ). (C to F) Total cellular RNA levels of VP1, and VP4 (SA11 panel) or NSP3 (RF panel) transcripts. Data are from three independent experiments. Dashed line represents detection threshold.

VP1 and VP4 viral transcripts. No marked differences in transcript levels of either VP1 (Fig. 3B) or VP4 (Fig. 3C) were observed ( $P \geq 0.05$ , paired  $t$  test).

Conversely, the NSP3 mutants followed similar replication kinetics to RF WT with three log<sub>10</sub> increases in titers between 8 and 16 hpi, with titers plateauing thereafter (Fig. 3D). Throughout, no major differences in titers between any of the viruses in the panel were observed. For the NSP3 virus panel, mutants produced higher levels of VP1 (Fig. 3E) and NSP3 (Fig. 3F) transcripts than the WT virus earlier in the time course. Higher RNA levels of VP1 and NSP3 in the RBD mutant are likely a result of higher RNA input (Fig. 3E and F, respectively). Possibly, a higher proportion of viral particles generated in the RBD virus stocks are nonviable, and therefore, more defective particles are present in the inoculum when equivalent PFU are used for the infections. Neither VP1

**FIG 2** Legend (Continued)

$P = 0.0005$ ). Data are from three independent experiments. Dashed line represents detection threshold. Viral titers and plaque morphology versus WT for VP4 (C and D) and NSP3 (E and F) mutants. Dashed line represents detection threshold. (C) \*,  $P \leq 0.05$  (RBM.1,  $P = 0.0205$ ; RBM.2,  $P = 0.0217$ ). \*\*,  $P \leq 0.01$  (HR2,  $P = 0.0018$ ). Representative results from three independent rescues are shown (except for RBD, which only rescued once). In panel E, open circles show failed rescues plotted at the limit of detection.

**TABLE 1** Properties of VP4 and NSP3 mutant viruses<sup>a</sup>

Viruses				Protein products of mutated gene			
Name	Titers (PFU/mL)	Total size of VP4 gene (bp)	Rescue success	VP4 size (aa)	VP4 size (kDa)	VP4 cleaved products	
						VP5* size (kDa)	VP8* size (kDa)
SA11 WT	1.65E + 08	2,331	3/3	776	86.1	60	28
HR2	2.25E + 06	2,430		809	89.8		31
NTD	4.75E + 06	2,400		799	88.7		30
RBM.1	2.75E + 06	2,400		799	88.7		30
RBM.2	2.50E + 06	2,412		803	89.1		30
Name	Titers (PFU/mL)	Total size of NSP3 gene (bp)	Rescue success	NSP3 size (aa)	NSP3 size (kDa)	T2A product/s (aa)	T2A product/s (kDa)
RF WT	1.30E + 08	942	3/3	313	34.7	n/a	n/a
RBM	1.10E + 08	1,158	2/3	385	42.7		
T2A_RBM	9.20E + 07	1,212	3/3	403	44.7	330 + 73	36.6 + 8.1
RBD	1.88E + 07	1,521	1/3	506	56.1	n/a	n/a
T2A_RBD	7.70E + 07	1,575	3/3	524	58.1	330 + 194	36.6 + 21.5

<sup>a</sup>The hypervariable region of SA11 VP4 was tagged with SARS-CoV-2 spike peptides: heptad repeat 2 (HR2), N-terminal domain (NTD), and receptor binding motif (RBM) regions. The C terminus of RF nonstructural protein (NSP) was tagged with either the RBM or receptor binding domain (RBD) of SARS-CoV-2 spike with or without a Thosasa asigna virus 2A (T2A) peptide; WT, wild type; n/a, not applicable.

nor NSP3 transcript levels differed significantly throughout the time course ( $P \geq 0.05$ , paired  $t$  test) (Fig. 3E and F).

Western blot analyses were then used to characterize the production of SARS-CoV-2 spike polypeptides and RV VP6 using whole-cell lysates from the infection time course. As different SARS-CoV-2 peptides were introduced in each mutant, antispike antibody affinity may vary between mutants and so expression levels cannot be compared. Due to lack of available antibodies, we were unable to measure RV VP4 and NSP3 protein levels directly.

For the detection of various SARS-CoV-2 spike peptides in cells infected with the VP4 mutants, a polyclonal SARS-CoV-2 spike antibody was used. As the spike peptides were introduced into the hypervariable region of VP4, we considered the possibility of detecting the full-length VP4 (sizes indicated in Table 1) and/or the VP8\* cleaved product containing the spike peptides. At 32 hpi, full-length VP4 product was detected in heptad repeat 2 (HR2), NTD, and RBM.2 mutants (Fig. 4A, black asterisks). No SARS-CoV-2 spike peptide signal was detected for the RBM.1 mutant, likely reflecting selective clonality of the antibody used (Fig. 4A). Interestingly, at 32 hpi, the upper band representing the uncleaved VP4 product was brighter for RBM.2 (Fig. 4A, black asterisks), whereas for NTD, the lower band possibly representing the VP5\* cleaved product was stronger than the upper band (Fig. 4A, green asterisks). These differences could be due to the distinct efficiencies of VP4 processing caused by the inserted peptides. The hypervariable region where the spike peptides were introduced is within the VP8\* domain, and we would expect a product of around 30 to 31 kDa in the event of VP4 cleavage. Possibly, this is evident in NTD at 32 and 48 hpi (Fig. 4A, blue asterisks), although the NTD mutant showed several unexpected bands and so this may reflect nonspecific antibody binding; a faint product of similar molecular weight was also detected in the mock samples at 32 hpi (Fig. 4A).

We also examined RV VP6 production, which was detected in all VP4 viruses at 32 hpi (Fig. 4A). VP6 signal intensity did not correlate with spike signal intensity across viruses, again likely due to variable affinities of the spike antibody for the different spike peptides incorporated into VP4 (Fig. 4A).

In cells infected with NSP3 mutants, detection of both RBD and RBM peptides was possible using a polyclonal SARS-CoV-2 RBD antibody. Cross-reactivity for the RBM-expressing virus was first detected at 8 hpi, with increased levels present at 16 and 32 hpi (Fig. 4B). Antibody cross-reactivity for the T2A\_RBM virus was only visible between 16 and 32 hpi (Fig. 4B). The band detected is consistent in size with an unseparated NSP3-T2A\_RBM protein product (Table 1 and Fig. 4B, black asterisks). The RBM peptide of around 10 kDa was not detected, consistent with its *in vitro* translation efficiency

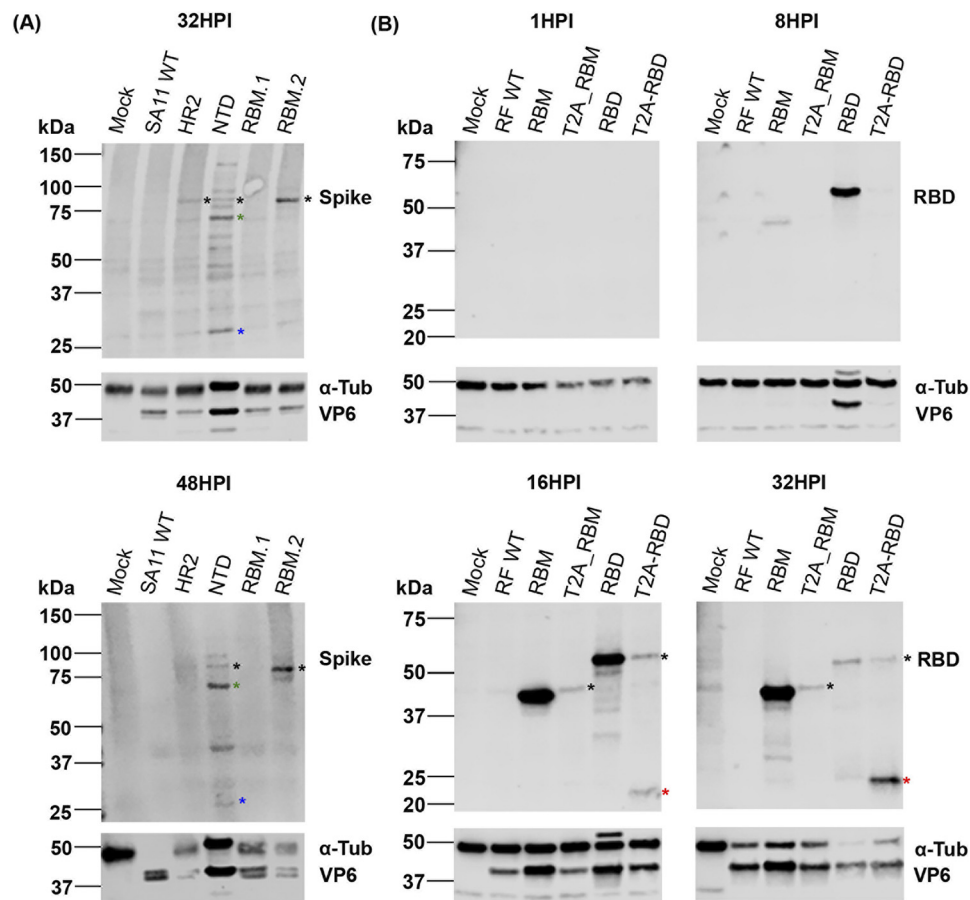


**FIG 4** Expression of VP6 and SARS-CoV-2 spike peptides in infected cells. Cells infected at low MOI were harvested at 1, 8, 16, 24, 32, and 48 hpi. Whole-cell lysates were analyzed by SDS-PAGE and Western blot using polyclonal antibodies against RV VP6, and spike for SA11 mutants (A) or RBD for RF mutants (B). Alpha-tubulin ( $\alpha$ -Tub) was used as a loading control. In panel A, black asterisks denote uncleaved VP4 product. Cleaved VP4 products VP5\* and VP8\* are marked by green and blue asterisks respectively. In panel B, black asterisks show T2A read-through product and red asterisks identify separated products. Representative results from three independent experiments are shown. Position of molecular weight markers are indicated (kDa).

(Fig. 4B and 1B). For the RBD virus, expression of the RBD peptide was first observed at 8 hpi but declined from 16 hpi paralleling the disappearance of tubulin (likely due to cell death) (Fig. 4B). In the T2A\_RBD mutant, both NSP3-conjugated and unconjugated RBD products were detectable from 16 hpi (Fig. 4B, black and red asterisks, respectively). Over time, the RBD peptide (~23 kDa) became more apparent, as the NSP3-RBD signal diminished, confirming the functionality of the T2A element (Fig. 4B, red asterisks).

It is unclear why the T2A-induced ribosomal skipping appeared to improve in efficiency over the course of infection. It is possible that the stability of the fused peptides is lower than the separated peptides. Similarly, over the course of infection, RBM protein levels increased throughout, whereas RBD protein levels increased until 16 hpi after which they dropped dramatically (Fig. 4B).

The expression of VP6 was first observed at 8 hpi during infection with the RBD mutant, coinciding with the signal of the RBD peptide, but was only detected for the remaining viruses from 16 hpi (Fig. 4B). Since equal MOIs were used for time course infections, higher input of genomic RNA copies could explain earlier V6 detection in the RBD mutant. This is consistent with the higher transcript levels detected for the RBD mutant at 8 hpi (Fig. 3E and F). It is possible that in the event of a packaging defect of the RBD mutant more input genome copies would be required to deliver equal numbers of infectious particles.

Infection with both mutants resulted in a similar drop in tubulin levels (Fig. 4A and B), suggesting that the two mutants have different protein turnover rates.

In summary, introducing short SARS-CoV-2 peptides into the hypervariable region of VP4 impacted the virus yield, whereas fusing SARS-CoV-2 spike peptides to the C terminus of NSP3 with or without T2A did not affect the virus titer or replication kinetics. Nevertheless, SARS-CoV-2 spike peptides were detectable in the majority of mutants using polyclonal antibodies, encouraging further investigations into the potential of these strategies for heterologous peptide presentation. Use of monoclonal SARS-CoV-2 spike antibodies could be considered in the future studies as these may be more specific for the detection of spike epitopes expressed by mutant viruses.

**Effect of gene mutation on viral genome packaging.** For viruses of the *Reoviridae* family, genome packaging is a tightly orchestrated and controlled process, so increasing the RV genome size may affect packaging efficiency (29, 67–69). To examine whether our mutations may have affected genome packaging, RNA was extracted from equal volume of purified viruses and analyzed by urea-PAGE and silver staining.

The VP4 virus panel showed the expected constellation of genome segments, but as samples were resolved for an extended period of time to visualize the small changes in segment 4 (VP4) band sizes expected as a result of SARS-CoV-2 spike peptide insertion, segments 10 and 11 ran off the gel (Fig. 5A). When gels were run for a shorter time, no differences in band densities of segments 10 and 11 were seen (data not shown). Mutated VP4 segments migrated more slowly than the WT VP4 segment, reflecting the various sizes of inserted spike sequences (Fig. 5A, highlighted in red). Densitometry analysis showed no substantial differences in band density between mutated VP4 and WT VP4 segments (normalized to WT: HR2 = 0.96, NTD = 1.11, RBM.1 = 0.87, and RBM.2 = 0.96), suggesting no obvious packaging defects were introduced by small sequence insertions into the hypervariable region of VP4 (Fig. 5A).

The resolved segments for the NSP3 virus panel also showed the expected pattern of 11 RNA segments, as well as a prominent background band present in a mock infected sample that migrated between segments 1 and 2 (Fig. 5B). Segment 7 (encoding NSP3) from all mutants migrated notably slower than from WT virus, corresponding with its increased gene size (Fig. 5B, highlighted in red). Comigration of segments 7, 8, and 9 in the WT made it difficult to reliably separate segment 7, precluding direct quantitative analyses (Fig. 5B). Nevertheless, no obvious defect in packaging was observed through visualization of the complete genome of RF mutants.

To further evaluate whether virion infectivity may have been affected by genome mutagenesis, the genome copy number to PFU ratio was determined for the two panels of viruses, measuring VP1 and either VP4 (SA11 panel) or NSP3 (RF panel) segments (Fig. 5C to F). No significant differences were observed in the levels of VP1 and VP4 segments across the VP4 mutants relative to WT, although for all mutants a 1 to 2 log<sub>10</sub> increase in RNA copies required to make an infectious virion was observed for both VP1 and VP4 ( $P \geq 0.05$ , paired  $t$  test) (Fig. 5C and D).

In contrast, all NSP3 mutants, with the exception of RBD, had equivalent numbers of VP1 and NSP3 segments (Fig. 5E and F). RBD had a significantly higher VP1 ( $P = 0.005$ , paired  $t$  test) and NSP3 ( $P = 0.010$ , paired  $t$  test) segment copy number:PFU ratio, with over 100-fold more copies of RNA required to make a fully infectious particle (Fig. 5C and D).

VP4 is important for viral attachment and entry as well as for the maturation of TLPs that constitute an infectious virus (3). Therefore, it was considered that mutation of VP4 may affect the assembly of the viral structural proteins. To test this, purified VP4 viruses were further analyzed by SDS-PAGE followed by Coomassie staining (NSP3 viruses were not included because the spike epitopes were fused to NSP3 which is not incorporated into virions) (Fig. 5G). Apart from VP3 and VP7 proteins, major structural proteins were detected throughout (Fig. 5G). VP4 was readily detectable for all viruses in the panel and so amounts were quantified by densitometry and normalized to that of WT virus. This showed no obvious VP4 incorporation defects, with all mutant viruses

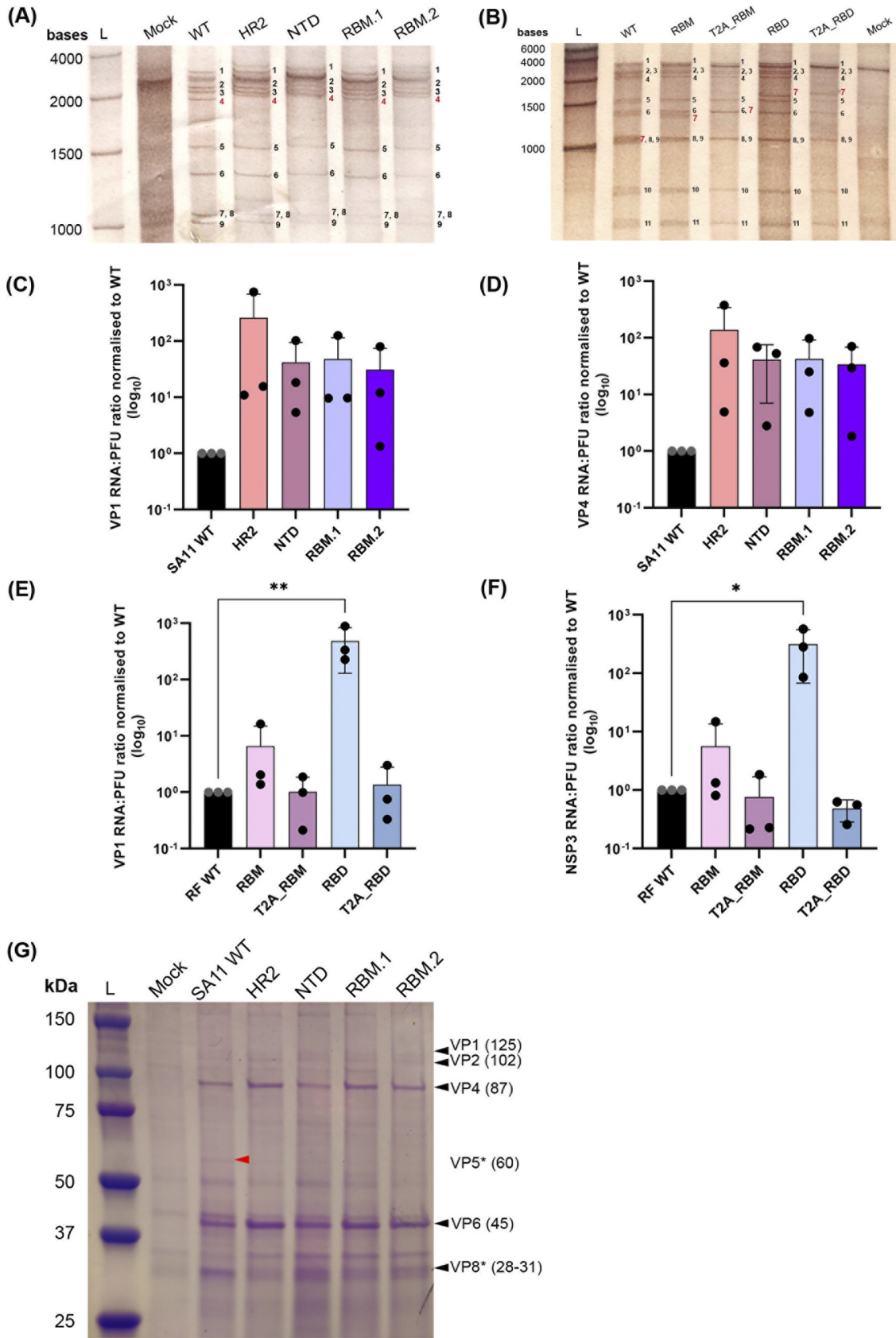


**FIG 5** Impact of VP4 and NP3 mutation on packaging of RV RNA and proteins. Extracted RNA from virus stocks was analyzed by urea-PAGE and silver staining for SA11 mutants (A) and RF mutants (B). Individual RNA segments are labeled in black, and mutated (Continued on next page)

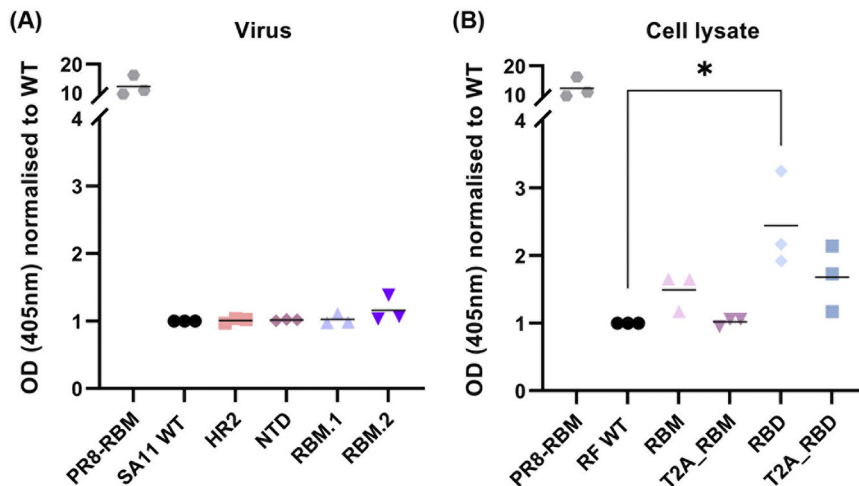


**FIG 6** Detection of spike antigens expressed by mutant viruses. Presence of spike antigens were evaluated by indirect ELISA using viral supernatant of VP4 mutants (A) and cell lysates for NSP3 mutants (B). Colored symbols represent individual data points obtained from three independent experiments. Optical density (OD) (405 nm) signal for all mutants was normalized to WT (background signal). PR8-RBM represents positive control. (A)  $P > 0.05$ . (B) \*,  $P \leq 0.05$  (RBD,  $P = 0.032$ ).

showing very similar VP4 amounts to the WT virus (relative to WT, values were as follows: HR2 = 1.07, NTD = 0.99, RBM.1 = 1.09, and RBM.2 = 1.06). Thus, the mutant VP4 proteins appear to be incorporated into virus particles with unaltered efficiency.

A notable difference between the WT virus and its mutants was the cleavage pattern of VP4 in the presence of trypsin used for propagating the panel of mutant viruses. A band of the predicted size for VP5\* was visible in the WT (Fig. 5G, red arrow). However, no corresponding band was visible for any of the VP4 mutants expressing heterologous peptides, further supporting our earlier hypothesis that peptide insertion into the VP4 hypervariable region impairs its processing into VP8\* and VP5\* (Fig. 4A).

In contrast, VP8\* was detected in all mutants, and it migrated slightly higher than WT VP8, corresponding to the additional peptide sequences present in the hypervariable domain of VP4 (Fig. 5G). Nevertheless, VP8\* band density was stronger for WT than for the mutants, again consistent with inefficient tryptic cleavage of VP4.

Overall, no major effect on viral assembly was observed in either of the mutant viral panels, with the exception of inserting the large RBD tag into NSP3, which caused a defect that could be overcome by incorporation of a T2A element.

**Detection of SARS-CoV-2 spike antigens by indirect ELISA.** To further investigate the viability of using RV as a delivery vector for SARS-CoV-2 spike antigens, we assessed whether the RV mutants expressing spike peptides would cross-react with RBD antibodies in an indirect ELISA. For the VP4 mutants, no antibody cross-reactivity was identified in this assay using the polyclonal SARS-CoV-2 RBD antibody (Fig. 6A). Additionally, no cross-reactivity was observed using the polyclonal SARS-CoV-2 spike antibodies to target the various spike peptides in the VP4 mutants, or with the PR8-RBM-positive control (data not shown), reflecting the lack of suitability of these antibodies for use in this assay.

Except the T2A\_RBM mutant, all NSP3 mutants consistently showed a higher signal than the background signal from the WT virus, although only the RBD mutant showed a significantly higher signal than WT ( $P = 0.032$ , paired  $t$  test) (Fig. 6B).

#### FIG 5 Legend (Continued)

RNA segment notations are in red. Lane "L" represents High Range RNA Ladder showing band size of RNA transcripts. RNA:PFU ratios of VP1 and either SA11 VP4 (C and D) or RF NSP3 (E and F) genes were determined by RT-qPCR and a ratio of copy number to viral titer was calculated; values were then normalized to WT. Dots represent individual samples from three independent rescues with each performed in triplicate. (E) \*\*,  $P \leq 0.01$  (RBD,  $P = 0.005$ ). (F) \*,  $P \leq 0.05$  (RBD,  $P = 0.010$ ). (G) Electrophoretic profile of viral proteins from purified VP4 mutants visualized using Coomassie brilliant blue. Lane "L" represents protein ladder indicating the molecular weight markers (kDa). Black triangles show the positions of viral proteins and their expected protein sizes (in brackets) are indicated (kDa). VP3 and VP7 proteins were not detected. VP5\* protein was detected in WT only (red triangle).

Based on these observations, RF NSP3 may be a better target for heterologous peptide conjugation than SA11 VP4 for expression of immunogenic antigens, which is at least partly attributable to the larger insertion site tolerated in the corresponding genome region.

**Bovine enteroids as a species-specific model for viral infection.** Cell culture-based assays identified the RF NSP3 gene as a strong candidate for expressing immunogenic heterologous peptides. Orally administered live attenuated RV vaccines replicate in the gastrointestinal tract, and so bovine intestinal organoids containing enterocytes, goblet, Paneth, enteroendocrine, and stem cells (70) were used to investigate if a more physiologically representative system was susceptible to infection with the NSP3 mutants. A bovine organoid system was chosen as the RF strain was first identified in diarrhoeic calves (71).

3D bovine enteroids were infected with NSP3 mutants at an approximate MOI of 10, stained with anti-VP6 and anti-RBD antibodies, and imaged by confocal microscopy (Fig. 7A and B, respectively). At 24 hpi, VP6 was predominantly detected in the epithelium comprised of mature enterocytes lining the apical surface of the organoid lumen (Fig. 7A), which is consistent with previous findings showing their preferential infection by RVs (17, 18). In contrast, VP6 distribution in RBM and T2A\_RBM mutants was detected around the nuclei of cells located within the organoid lumen and in the punctate cytoplasmic inclusion bodies, most likely viroplasms, sites of RV replication and assembly (3) (Fig. 7A, VP6 panel). However, antibodies targeting NSP2 and NSP5 proteins, which together are necessary and sufficient for the formation of viroplasms (72), are not commercially available and so viroplasm identification could not be verified. VP6 signal in the RBD and T2A\_RBD mutants was not apparent in the lumen and was mainly detected around the nuclei of cells in the organoid lining (Fig. 7A, VP6 panel).

Following staining with the SARS-CoV-2 RBD antibody, diffuse cytoplasmic signal was detected in a small number of cells of organoids infected with the RBM mutant, while other mutants did not produce any visible anti-RBD cross-reactivity (Fig. 7B). However, the signal for RBM was weak relative to the background, indicating either that the expression of SARS-CoV-2 spike peptides was hindered in bovine enteroids or that the antibody does not work well in this context.

## DISCUSSION

We have used simian SA11 and bovine RF RV strains as viral vectors to express various SARS-CoV-2 spike epitopes as a model system with which to test the potential for expression of multivalent antigens. Tagging of the VP4 protein found on the surface of the virion with smaller peptides consistently impaired viral growth and did not yield strong antibody cross-reactivity. Conversely, relatively large foreign sequences could be tagged to the C terminus of NSP3 protein, mostly without impairing viral titers and replication kinetics, and cross-reactivity with SARS-CoV-2 RBD antibodies was also demonstrable.

To investigate the feasibility of using RV as an expression vector, we analyzed the effect of introducing SARS-CoV-2 spike peptides into the “head” region of the VP4 (i.e., VP8\* domain), outside the sialic acid binding domain. Since VP8\* is used in several vaccine platforms such as protein subunit or nanoparticle vaccines to induce RV-specific neutralizing antibodies (73–78), we hypothesized that the expression of SARS-CoV-2 spike peptides by VP8\* may similarly generate neutralizing antibodies. However, incorporation of various spike epitopes into the VP8\* lectin domain between amino acid positions 164 to 198 consistently showed significant decrease in viral titers, despite having no obvious effect on the rescue efficiency (Fig. 2C).

It is possible that reduced infectivity and lack of uniformity of plaque sizes of VP4 mutants (Fig. 2C and D and Fig. 3A) could be due to inefficient conformational transition of VP4 following proteolytic cleavage (3, 20, 21). Following cell attachment, VP8\* lectin domains at the tip of VP4 dissociate and expose the hydrophobic loops of the VP5\*  $\beta$ -barrel domains (19, 63, 64). This enables interaction of the VP5\* hydrophobic loops with the lipid bilayer and perforation of the target membrane by the VP5\* foot

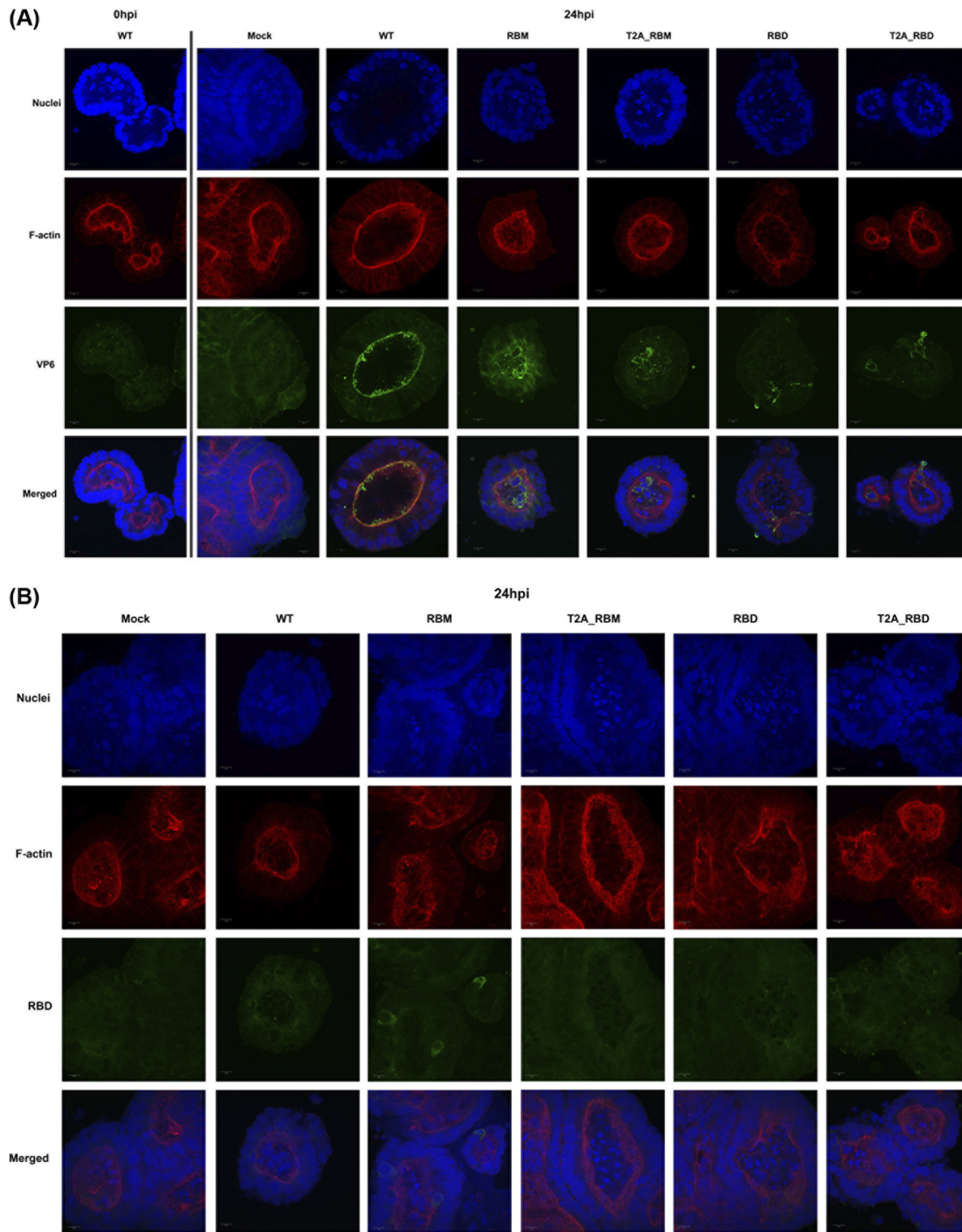


**FIG 7** Bovine enteroids infected with NSP3 mutant viruses. Three-dimensional bovine enteroids were infected with the panel of NSP3 mutants, or mock at an approximate multiplicities of infection of 10 PFU per cell and fixed at 24 hpi, or at 0 hpi for WT as a control for background signal. Cells were stained for RV VP6 (A) and RBD of SARS-CoV-2 spike (B). Scale bar represents 10  $\mu$ m.

domain, leading to RV entry, analogous to refolding of influenza virus hemagglutinin during membrane fusion (63, 64, 79–84). Therefore, our mutation of the VP8\* lectin domain may have indirectly affected the association of the hydrophobic loops of the VP5\*  $\beta$ -barrel domains with the target membrane.

Alternatively, while we saw no obvious effects of VP4 mutagenesis on genome packaging (Fig. 5A, C, and D), the absence of the VP5\* detection in the mutants (where a band of the correct size was identified in the WT virus) could indicate inefficient cleavage of VP4 on TLPs (Fig. 5G). *In vitro* assembly of TLPs has shown that DLPs require addition of VP4 before VP7, and that the tryptic cleavage occurs following addition of VP7 (82, 85). Interaction of VP7 subunits with the VP5\* foot domain stabilize and anchor the VP4 onto the virion, allowing the protease to cleave only the linker sequence that bridges VP8\* and VP5\*, which in our mutants is intact (20, 21, 63, 64). It is possible that our peptide insertions may have altered the VP4 conformation at this interaction site, disrupting VP4 cleavage and rendering VP5\* undetectable in our assays (Fig. 4A and 5G). Finally, we were unable to detect any cross-reactivity of the SARS-CoV-2 spike peptides with spike (not shown) or RBD antibodies in ELISA (Fig. 6A), further suggesting limitations of using SA11 VP4 as an expression vector for foreign peptides, at least with the chosen peptides. It is possible, however, that these peptides may be immunogenic *in vivo*, which could be tested in a suitable animal model such as mice (86). Using a multiplexed approach, challenge with a combination of VP4 mutants could be applied to establish a more robust SARS-CoV-2 specific immune response.

Previous studies have shown that SA11 NSP3 is able to tolerate insertions of foreign sequences at its C terminus (45, 51, 52); we have demonstrated that this is also possible using the bovine RF strain NSP3. This is advantageous as the current live attenuated pentavalent RV vaccine RotaTeq utilizes a bovine RV backbone reassorted with different human strains, and the use of a nonprimate origin RV vector would lower susceptibility to preexisting immunity (9, 87, 88). In contrast, a monovalent, human live attenuated RV vaccine Rotarix contains only one RV strain of G1P[8] specificity (89, 90). The bovine backbone is amenable to multiplexing, and therefore will offer a broader protective immunity than those containing one specific RV strain.

The RF strain of RVs demonstrates a positive feedback mechanism for NSP3 mRNA translation where the 3'-GACC end of mRNA molecules and both domains (N and C terminal) of NSP3 are required (91). Accumulation of the first NSP3 molecules generated during infection triggers NSP3-dependent translation by specifically binding the terminal 3' GACC of mRNA, and once established, NSP3 is available for translation of other viral mRNAs (91). Depending on the virus strain, the 3'-GACC canonical sequence differs in some segments of RV, and the same positive feedback mechanism is not observed in the SA11 strain (3, 91).

Rescue of the RF mutant with the RBD peptide (193 amino acids) fused directly to NSP3 was achieved only once in three attempts (Fig. 2E), possibly reflecting an impaired function of NSP3. However, introducing the RBM peptide produced a virus of similar titers to the WT and its rescue efficiency was not as affected (Fig. 2E). The only notable difference between the RBM and RBD was the size of the introduced peptide, suggesting that insertions larger than 72 amino acids may affect the function of NSP3. Increasing the size of the ORF by incorporating the T2A element improved the titer and the rescue efficiency of the T2A\_RBD mutant (Fig. 2E), suggesting that the rescue defect imparted by peptide introduction is at the protein rather than the RNA level. Previous studies showed that inclusion of the porcine teschovirus 2A element (P2A) between SA11 NSP3 ORF and the coding sequence for UnaG resulted in NSP3 retaining its ability to induce nuclear localization of PABP (51). These recombinant viruses expressed both NSP3 and UnaG proteins, and grew to peak titers similar to those of SA11 WT (45, 51). Recombinant simian rhesus rotavirus (RRV) strain expressing green fluorescent protein from NSP3 C terminus, separated by P2A element, also had comparable growth kinetics to the WT virus (44). However, a more recent study showed that

the titers of recombinant SA11 RVs expressing SARS-CoV-2 peptides from the C terminus of NSP3 ORF with P2A were 0.5 to 1 log lower than the WT (52). Furthermore, the recombinant SA11 RV expressing the whole of SARS-CoV-2 spike from NSP3 with P2A showed genetic instability (by passage three) in which sequence deletions were apparent with continued passage (52). Our results confirm that introducing peptides to the C terminus of NSP3 separated by the T2A element did not affect the function or genetic stability of NSP3 (Fig. 2E, 4B, and 5B). In the absence of a T2A element, there may be a limit to the length of additional foreign sequences that the bovine RF NSP3 can accommodate. However, it is not possible to rule out that the activity of different 2A elements and the effects of different RG systems used for viral rescue can vary (44, 45, 51, 52, 66).

We also found that the RNA:PFU ratios as well as the copy number of NSP3 and VP1 transcripts were affected for the RBD mutant only, suggesting that a higher proportion of viral particles generated are nonviable (Fig. 5E and F). This cannot be attributed to the longer length of this segment, as the T2A\_RBD mutant did not have a raised RNA:PFU ratio (Fig. 5E and F). A higher number of defective virions in the viral progeny may explain the variable plaque sizes of NSP3 mutants (Fig. 2F). NSP3 exerts its role in virus replication by regulating viral mRNA translation. This is consistent with the observed increase in RNA:PFU ratios being nonspecific to a particular segment.

With the exception of T2A\_RBM, NSP3 mutants expressing SARS-CoV-2 spike peptides cross-reacted with the SARS-CoV-2 RBD antibody (Fig. 6B), supporting the previously proposed viability of using NSP3 as a tagging system (52) and demonstrating its application to other RV strains. Follow up studies using sera from COVID-19 patients are needed to confirm antibody responses to the antigens produced by the NSP3 mutants.

Overall, we conclude that further investigation is required to evaluate the potential for peptide insertion into VP4 as a potential vaccine expression platform, using animal models to examine immunogenicity. Here, small peptide insertions into VP4 resulted in a log reduction in virus titer, which is tolerable when we consider other live attenuated vaccines currently in use, such as the influenza A vaccine FluMist (reviewed in reference 92). On the other hand, including the T2A element is beneficial for expressing foreign antigens as it allows coexpression of NSP3 and large peptides with little effect on the viral rescue efficiency, titer, and replication, all which are important traits for live attenuated vaccine development. In the absence of the T2A element, there may be a limit to the amount of additional foreign sequences that the RF NSP3 can accommodate. Nevertheless, there is potential to package additional heterologous peptides into the RV core, which may be several thousands of nucleotides in excess of the native dsRNA genome (93). Our results offer a possibility of utilizing a bovine RV RF strain as a backbone to facilitate the development of recombinant RV-based vaccines; here we used SARS-CoV-2 as an example, but this can be extrapolated to other gastrointestinal pathogens.

## MATERIALS AND METHODS

**Cell lines.** African Green monkey kidney epithelial (MA104) cells were cultured in Dulbecco's modified Eagle's medium (DMEM) (Sigma-Aldrich) supplemented with heat inactivated 10% fetal bovine serum (FBS) (Gibco) and 1% penicillin-streptomycin (Gibco). Cells of the BSR-T7 clone of baby hamster kidney fibroblasts (BHK-21 cells) (94), constitutively expressing T7 RNA polymerase, were cultured in Glasgow's minimal essential medium (Gibco) supplemented with 1% tryptose phosphate broth (Gibco), heat inactivated 10% FBS (Gibco), and 1% penicillin-streptomycin (Gibco). Both cell lines were a kind gift from the laboratory of Prof. Massimo Palmarini (MRC-University of Glasgow Centre for Virus Research, UK). Cells were passaged twice weekly and maintained at 37°C, 5% CO<sub>2</sub>. At every fifth passage, BSR-T7 cells were maintained in medium containing G-418 selection (1 mg/mL) (Invitrogen).

**Viruses.** RV strains used were simian RV SA11 strain (G3P[2]) and bovine RV RF strain (G6P[1]) and were rescued using reverse genetics (detailed below) (42, 71, 95, 96). The natural isolate of the RF strain was a kind gift from the laboratory of Dr. Ulrich Desselberger (University of Edinburgh, UK). Viruses were propagated in MA104 cells cultured in DMEM supplemented with 0.5 µg/mL porcine pancreatic trypsin type IX (Sigma-Aldrich), and viral titers were measured by plaque assay as described below.

**Design of RV expression vectors containing spike epitopes.** To engineer mutant RVs expressing SARS-CoV-2 spike peptides, we utilized two strategies involving both the simian RV SA11 strain and the

bovine RV RF strain. It was previously suggested that the surface protein VP4 of the SA11 strain tolerates short immunogenic peptides inserted at specific sites with minimal impact on viral replication or particle assembly (79). Guided by the available structure model of rhesus rotavirus (RRV) VP4, serotype G3 P5B[3] (strain RVA/Monkey/United States/RRV/1975/G3P5B[3]) (PDB: 4V7Q) (63), we chose an exposed loop outside the sialic acid-binding domain located within the "head" of the VP4 spike (Fig. 1A and B) to investigate the possibility of VP4 alteration. Moreover, several neutralization escape mutants were ascribed to the amino acid changes within this region (97), consistent with its accessibility to antibodies. A number of B-cell linear epitopes derived from either the heptad repeat 2 (HR2), N-terminal domain (NTD), or RBM regions of the SARS-CoV-2 spike protein were selected for insertion (61, 98, 99) (Fig. 1A). These epitopes were introduced into the hypervariable region of SA11 VP4 between amino acid position 164 and 198 with linker sequences (63, 64) to increase their accessibility. Plasmid constructs expressing HR2 and NTD of the SARS-CoV-2 spike peptides were generated using Q5 site-directed mutagenesis kit (New England Biolabs) with primers listed in Table 2 and pT7-VP4SA11 (Addgene no. 89165) expression vector according to the manufacturer's protocol. RBM.1 and RBM.2 constructs were ordered as gene fragments (gBlocks; Integrated DNA Technologies) and cloned into pT7-VP4SA11 expression vector using NheI and MfeI restriction enzymes. All plasmids were amplified by transformation into chemically competent *Escherichia coli* DH5 $\alpha$  and purified using Qiagen Plasmid Midi Kit (Qiagen) according to the manufacturer's protocol. The presence and the size of the mutation in each plasmid was verified by Sanger sequencing (GATC Biotech or Genewiz, Germany). These epitopes were curated from the scientific literature by the Immune Epitope Database available at VIPR (<https://www.viprbrc.org/brc/>). Only unstructured epitopes of up to 15 residues were chosen (Table 3). The SA11 strain was selected for this mutagenesis due to the structural characterization of VP4 of its close relative RRV, its user-friendly plasmid only-based reverse genetics system and its rapid growth kinetics.

To test whether tagging a RV strain more closely related to the bovine virus backbone used in the pentavalent RotaTeg vaccine (87), we used the bovine RV RF strain. Here we modified the C terminus of the RF strain NSP3 ORF to express spike epitopes coding for the RBD or RBM of SARS-CoV-2, with or without an intervening *Thossea asigna* virus 2A (T2A) peptide (66, 100, 101) (Fig. 1A). The inclusion of the T2A sequence was employed in order to lower the risk of interfering with the function of the NSP3 gene. On the other hand, increasing the segment size by incorporating the T2A peptide could further affect the antigenic processing; hence, both approaches were trialed. The panel of constructs was assigned the notation RBM, T2A-RBM, RBD, and T2A-RBD.

**Plasmid construction.** pT7 plasmids used for reverse genetics of SA11 RV were kindly provided by Takeshi Kobayashi (42) through the Addgene plasmid repository under ID number 89162-72. To generate plasmids used for reverse genetics of the bovine RV RF strain, constructs were designed to encode each of the 11 RF gene segments, flanked at the 5' end by a T7 promoter (T7P) and at the 3' end by an antigenomic hepatitis delta virus ribozyme sequence, followed by the T7 terminator sequence as in Kanai et al. (42). The GenBank accession numbers of the bovine RV RF strain genome sequences are as follows: segment 1 (KF729687), segment 2 (KF729642), segment 3 (KF729645), segment 4 (KF729650), segment 5 (KF729656), segment 6 (KF729658), segment 7 (KF729664), segment 8 (KF729667), segment 9 (KF729675), segment 10 (KF729677), and segment 11 (KF729684) (96). The constructs were synthesized by Invitrogen GeneArt on either pMK-RQ (kanamycin resistance), pMA-RQ, or pMA-T (ampicillin resistance) vectors. RF strain NSP3 constructs RBM, T2A-RBM, RBD, and T2A-RBD were ordered as gene fragments from Invitrogen GeneArt and cloned into pT7-NSP2SA11 expression plasmid (Addgene no. 89169) after the NSP2 ORF was removed using SmaI and Sall restriction enzymes. All plasmids were amplified by transformation into chemically competent *E. coli* DH5 $\alpha$ , except for the RF VP7 encoding plasmid for which DH10 $\beta$  cells were used, and purified using Qiagen Plasmid Midi Kit (Qiagen) according to the manufacturer's protocol. The presence and the size of the mutation in each plasmid were verified by Sanger sequencing (GATC Biotech or Genewiz, Germany) using primers listed in Table 2. Sequence results were analyzed in SSE v1.2 software (102).

**In vitro transcription and translation assay.** Coupled *in vitro* transcription and translation reactions were carried out using the Promega TnT Coupled Reticulate Lysate System labeled with radioactive [ $^{35}$ S] methionine (PerkinElmer Inc.) according to the manufacturer's protocol. Briefly, TnT reactions were set up as follows: 8  $\mu$ L TnT mix, 1  $\mu$ Ci [ $^{35}$ S]methionine, and 200 ng plasmid DNA, made up to 10  $\mu$ L with H $_2$ O. Mixes were prepared on ice before reactions were incubated at 30°C for 90 min. The reactions were denatured in 8.5  $\mu$ L of 2 $\times$  Laemmli buffer (65.8 mM Tris-HCl [pH 6.8], 100 mM DTT [pH 6.8], 2.1% sodium dodecyl sulfate [SDS], 26.3% [wt/vol] glycerol, 0.01% bromophenol blue) and boiled for 10 min at 95°C. Samples were analyzed using SDS-PAGE and autoradiography.

**Autoradiography of dried polyacrylamide gels.** Gels were fixed in gel fixing solution (50% [vol/vol] methanol in water with 10% [vol/vol] acetic acid) on a rocker for 45 min with the gel fixing solution being replaced every 15 min. Fixed gels were transferred onto 3MM Whatman filter paper (Scientific Laboratory Supplies), covered with cling film and dried in a gel dryer (model 543; Bio-Rad) by heating up to 80°C for 2 h under vacuum. Dried gels were placed in a sealed cassette with an X-ray film (Fisher Scientific) overnight. X-ray films were developed using a Konica SRX-101A X-ray film processor following manufacturer's protocol.

**Reverse genetics system.** Viruses were rescued using a combination of the protocols described by Kanai et al. (42) and Komoto et al. (43), with slight modifications. At 70% confluence, monolayers of BSR-T7 cells in 6-well plates were cotransfected with 11 plasmids corresponding to each RV genome segment (2.5  $\mu$ g for plasmids encoding NSP2 and NSP5; 0.8  $\mu$ g for the remaining plasmids) and plasmids encoding two vaccinia virus capping enzyme subunits (pCAG-D1R and pCAG-D12L: 0.8  $\mu$ g each) using 16  $\mu$ L Lipofectamine 2000 (Invitrogen) per transfection reaction in a total volume of 200  $\mu$ L of Opti-MEM

**TABLE 2** Names and nucleotide sequences of primers used in this study<sup>a</sup>

Target gene	Primer name	Sequence (5' to 3')	Use	Expected size of amplicon (bp)
SA11 VP4 in HR2 mutant plasmid	T7_FW	TAATAGCACTCACTATATAGGG	Sequence pT7-VP4SA11 plasmid containing SARS-CoV-2 HR2 peptide	2,517
	VP4_559_F	GCTAGGACAGCACATTATTC		
	HDV_REV	TCGTCACCTCGGATGGCTA		
HR2 of SARS-CoV-2 spike	FW	GATTCATTTAAATTTTTAGCGACCTCATTGAGGCGGT	Site-directed mutagenesis of HR2 peptide	n/a
	REV	CAATTTCCGGAAGTTGTTTTACGACATCAATAAATTC		
NTD of SARS-CoV-2 spike	FW	ACTCATTGACCTTCAAGAAATGGGAAAAATATGAGCA	Site-directed mutagenesis of NTD peptide	n/a
		ATATGGAGCTAGCGCAAAATGGAAAGTATAGGACA		
	ATATG			
	TAAATTCCTTTGTCAATCTCAAAGCTCTTCCGGGAGTT			
REV	GTTTTACGACATCAATAAATTC			
	CCAGACTCTAAATTCAGGGTTGTTGGAGCTAGCG			
SA11 VP4	SA11_VP4_1F	CAAATGGAAAGTATAGGACAAATATG	Sequence pT7-VP4SA11 plasmids containing SARS-CoV-2 spike peptides; PCR and Sanger sequencing of SA11 VP4 gene in viruses	1,192–1,275
		GGCTATAAAATGGCTTCGCTC		
		GTCTACCAGTTGGACAATGGC		
SA11 VP4	SA11_VP4_FWD	CATCAGCATGGACGGATGTAT	RT-qPCR of SA11 VP4 gene	83
		CCTCAGTTTGTGGCCATTC		
SA11 VP1	SA11_VP1_448F	GCAGTCATGTTCTGGTTGGA	RT-qPCR of SA11 VP1 gene	89
		GTTATGCCTTGGTACGCCAT		
RF NSP3	SA11_VP1_576R	CGGTTGGCCGATTCATTAAT	Sequence RF NSP3 plasmids	1,769–2,186
		FW_331		
		HDV_REV		
SARS-CoV2_FW	SARS_CoV2_REV	GCTTTTCAGTGGTTGATGCT	PCR and Sanger sequencing of RF NSP3 gene in viruses	1,178–1,595
		TCATAGAGGTCATGTGAAG		
		GATGCTCAAGATGGAGTCTAC		
REV_NSPP3_qPCR	REV_NSPP3_qPCR	CACCTGAATCATCCATTAGT	RT-qPCR of RF NSP3 gene	134
		CACAATCCGAGTTCAAATTC		
RF VP1	REV_RE_VP1_qPCR	CAGTGTGGCATTCTCCATAAC	RT-qPCR of RF VP1 gene	119

<sup>a</sup>VP, viral protein; n/a, not applicable.

**TABLE 3** SARS-CoV-2 spike amino acid sequences selected for insertion (61, 98, 99) into the hypervariable region of SA11 VP4 and tagging of RF NSP3<sup>a</sup>

SARS-CoV-2 peptide insertions	Amino acid sequence (N to C terminal)
SA11 VP4 construct	
HR2	EIDRLNEVAKNLESIDLQELGKYEQY
NTD	KSFEIDKGIYQTSNFRVW
RBM.1	SNNLDSKVGGNYNLYRL
RBM.2	FRKSNLKPFFERDISTEIQAGS
RF NSP3 construct	
RBM	NSNNLDSKVGGNYNLYRLFRKSNLKPFFERDISTEIQAGSTPCNGVEGFNCYFPLQSYGFQPTNGVGYQPY
T2A_RBM	<u>EGRGSLTTCGDVEENPGP</u> NSNNLDSKVGGNYNLYRLFRKSNLKPFFERDISTEIQAGSTPCNGVEGFNCYFPLQSYGFQPTNGVGYQPY
RBD	LCPFGEVFNATRFASVYAWNRKRISNCVADYSVLVNSASFSTFKCYGVSPTKLNLDLFTNVDYVIRGDEVRQIAPGQTGKIADYNYKL PDDFTGCVIAWNSNNLDSKVGGNYNLYRLFRKSNLKPFFERDISTEIQAGSTPCNGVEGFNCYFPLQSYGFQPTNGVGYQPYR <sup>66</sup> VVLL SFELLHAPATVCGP
T2A_RBD	<u>EGRGSLTTCGDVEENPGP</u> LCPFGEVFNATRFASVYAWNRKRISNCVADYSVLVNSASFSTFKCYGVSPTKLNLDLFTN VDYVIRGDEVRQIAPGQTGKIADYNYKL PDDFTGCVIAWNSNNLDSKVGGNYNLYRLFRKSNLKPFFERDISTEIQAGSTPC NGVEGFNCYFPLQSYGFQPTNGVGYQPYR <sup>66</sup> VVLLSFELLHAPATVCGP

<sup>a</sup>Sequence of the T2A peptide (66) is underlined.

(Gibco). After 24-h incubation at 37°C 5% CO<sub>2</sub>, MA104 cells (1 × 10<sup>5</sup> cells/well) were added to transfected BSR-T7 cells and cocultured for 4 days in FBS-free DMEM supplemented with 0.5 μg/mL porcine pancreatic trypsin type IX. Cocultured cells were then lysed three times by freeze/thaw and lysates were incubated with trypsin at a final concentration of 10 μg/mL for 30 min at 37°C 5% CO<sub>2</sub> to activate the virus. Lysates were then transferred to fresh MA104 cells in T25 flasks and incubated at 37°C 5% CO<sub>2</sub> for 1 h. After adsorption, MA104 cells were washed and cultured in FBS-free DMEM supplemented with 0.5 μg/mL porcine pancreatic trypsin type IX for up to 7 days or until complete cytopathic effect was observed. Cells were then lysed three times by freeze/thaw, pelleted at 3,220 × g for 30 min and virus-containing supernatants (P1 stocks) were aliquoted and stored at -80°C. To generate mutant SA11 or RF mutant viruses, plasmids encoding either the SA11 VP4 or RF NSP3 gene segment were replaced with corresponding plasmids encoding SARS-CoV-2 spike epitopes. Mock preparations with the mutated segment omitted were generated for use as negative controls throughout. All rescue experiments were performed three times for each virus panel. NSP3 mutants were passaged in cells up to five times maintaining stable transgene expression (confirmed by Sanger sequencing, data not shown). The panels of viruses were titred by plaque assays, and the presence of mutations in the target gene segments was confirmed by RT-PCR and Sanger sequencing (GATC Biotech or Genewiz, Germany) as described below. Properties of mutant viruses are summarized in Table 1.

**RT-PCR.** RNA was purified from viral stocks using the spin protocol of the QIAamp Viral RNA minikit (Qiagen) followed by RQ1 RNase-Free DNase treatment (Promega) to remove possible plasmid contamination according to the manufacturer’s specifications. cDNA was synthesized with SuperScript III Reverse Transcriptase (RT) kit (Invitrogen) using 5 μL RNA and 1 μL random hexamer primers (10 μM) (Invitrogen) according to the manufacturer’s protocol. PCR was then used to amplify across the regions containing the SARS-CoV-2 spike epitopes in SA11 VP4 or RF NSP3 with primers listed in Table 2 (amplicon product sizes: ~1.2 to 1.6 kbp). Using the Q5 High-Fidelity DNA polymerase PCR Kit (New England BioLabs) for SA11 VP4 and Platinum Taq DNA polymerase (Invitrogen) for RF NSP3, PCRs were set up according to the manufacturer’s instructions in a T100 Thermal Cycler (Bio-Rad). SA11 VP4 PCR conditions were 1 cycle of 98°C for 30 sec, followed by 35 cycles of 20 sec at 98°C, 20 sec at 52°C, and 2 min at 72°C, finishing with a 2 min incubation at 72°C. RF NSP3 PCR conditions were 1 cycle of 5 min at 95°C, followed by 35 cycles of 30 sec at 95°C, 30 sec at 55°C, and 2 min at 72°C, finishing with a 5-min incubation at 72°C. PCR product length was confirmed by 0.8% agarose gel electrophoresis containing SYBR Safe DNA Gel Stain and gels were imaged using the Odyssey XF imaging system (LI-COR). Analyses were performed with Image Studio Lite software (LI-COR). The presence of sequence insertions was confirmed by sequencing at GATC Biotech or Genewiz, Germany using primers listed in Table 2. Sequence results were analyzed in SSE v1.2 software (102).

**Plaque assay.** Plaque assays for RV infectivity were performed using adapted methods (103, 104). In brief, confluent monolayers of MA104 cells in 6-well plates were washed with FBS-free DMEM and infected with 800 μL of 10-fold serially diluted virus for 1 h at 37°C 5% CO<sub>2</sub>. Following virus adsorption, 2 mL/well overlay medium was added (1:1 ratio of 2.4% Avicel [FMC Biopolymer] and FBS-free DMEM supplemented with 0.5 μg/mL trypsin type IX) and incubated for 4 days. Cells were then fixed for 1 h with 1 mL/well of 10% neutral buffered formalin (CellPath) and stained for 1 h with 0.1% Toluidine blue (Sigma-Aldrich) dissolved in H<sub>2</sub>O.

**Multistep virus growth kinetics.** To compare growth kinetics of WT and mutant viruses, monolayers of MA104 cells at 70% confluence in 24-well plates were infected in technical triplicate with viruses at a multiplicity of infection (MOI) of 0.03 PFU/cell. A low MOI of 0.03 was selected to permit multiple cycles of infection. After 1 h, cells were washed three times with FBS-free DMEM and cultured with FBS-free DMEM supplemented with 0.5 μg/mL trypsin type IX. Viral supernatant and whole cell lysates were harvested at 1, 8, 16, 24, 32, and 48 h postinfection (hpi) and frozen at -80°C. Virus titers were

**TABLE 4** Primary and secondary antibodies used in this study<sup>a</sup>

Antibody	Catalog no. (supplier)	Clonality/host species or conjugate	Dilution	Used in
Primary antibody				
RV VP6	Ab181695 (Abcam)	Monoclonal/mouse	1 in 1,000	Western blotting Immunofluorescence
Alpha-tubulin	NB600-506 (Novus Biologicals)	Monoclonal/rat	1 in 5,000	Western blotting
SARS-CoV-2 Spike Protein	DA123 (MRC protein phosphorylation and Ubiquitylation unit, Dundee)	Polyclonal/sheep	1 in 100	
SARS-CoV-2 Spike RBD	PA5-114451 (Invitrogen)	Polyclonal/rabbit	1 in 100 1 in 1,000 1 in 1,000	ELISA Immunofluorescence Western blotting
Secondary antibody				
Donkey anti-mouse	A32766 (Invitrogen)	Alexa Fluor 488	1 in 1,000	Immunofluorescence
Donkey anti-mouse	926-32212 (LI-COR)	Alexa Fluor 800	1 in 10,000	Western blotting
Goat anti-rat	926-68076 (LI-COR)	Alexa Fluor 680	1 in 10,000	
Rabbit anti-sheep	SA5-10060 (Invitrogen)	Alexa Fluor 800	1 in 10,000	

<sup>a</sup>RV, rotavirus.

determined by plaque assay. Whole cell lysates harvested in 350  $\mu$ L buffer RLT (Qiagen) were used to determine the RNA concentration by quantitative RT-PCR (RT-qPCR) (see below) and lysates harvested in 100  $\mu$ L 2 $\times$  Laemmli buffer were used to analyze protein expression by Western blotting as described below.

**Viral RNA extraction and quantification by RT-qPCR.** Primers for RT-qPCR targeting segments VP1 (SA11 and RF), VP4 (SA11), and NSP3 (RF) were designed using SSE v1.2 and OligoCalc software (102, 105) (Table 2).

RNA was extracted from infected cell lysates using RNeasy minikit (Qiagen) with an on-column DNase treatment (Qiagen) to remove possible DNA contamination according to manufacturer's specification. The extracted RNA was dissolved in 20  $\mu$ L nuclease-free water (Qiagen) and stored at  $-80^{\circ}\text{C}$ .

To quantify total RNA levels of each segment relative to WT from time course experiments, one-step RT-qPCR was performed using SensiFAST SYBR Lo-ROX One-Step Kit (Meridian Bioscience) with 2  $\mu$ L of RNA samples according to the manufacturer's protocol on a Rotor-Gene Q apparatus (Qiagen) using primers listed in Table 2. RT-qPCR cycling conditions were:  $45^{\circ}\text{C}$  for 10 min for reverse transcription, 2 min at  $95^{\circ}\text{C}$ , followed by 40 cycles of 10 sec at  $95^{\circ}\text{C}$  and 30 sec at  $60^{\circ}\text{C}$ . The conditions then increased from  $50^{\circ}\text{C}$  to  $99^{\circ}\text{C}$  at  $1^{\circ}$  increments to generate a melting curve to confirm specific amplification of each gene. For relative expression of each gene, the results were analyzed according to the  $2^{-\Delta\text{Ct}}$  method (106). Average threshold cycle ( $C_{\text{T}}$ ) values of each gene were normalized to WT at 8 hpi (when RNA was first reliably detected for VP1, VP4, and NSP3), and the resulting  $\Delta C_{\text{T}}$  values were adjusted for primer efficiency. Three independent experiments were performed in technical duplicates.

To quantify the RNA copies of corresponding gene segments in mutant viruses for RNA:PFU ratios, RNA from cDNA (approximately 100 ng) of each gene segment was synthesized using a MEGAscript T7 transcription kit (Invitrogen) followed by TURBO DNase treatment (Invitrogen) and a cleanup with MinElute PCR purification kit (Qiagen) according to manufacturer's instructions. The extracted RNA was dissolved in 10  $\mu$ L nuclease-free water (Qiagen) and stored at  $-80^{\circ}\text{C}$ . RNA was measured using Qubit RNA broad range assay kit (Invitrogen) and serial dilutions of RNA were used as standards in one-step RT-qPCR. A ratio of the transcript copy number of each gene segment in the mutant viruses to virus titer was calculated and normalized to WT. Three independent experiments were performed in technical triplicates with the standard done in duplicate.

The PCR efficiency (E) of each primer pair set was established by measuring serial dilutions of cDNA of each segment in triplicate and calculated based on the slope of the standard curve according to the formula  $E = [10^{(-1/\text{slope})-1}] \times 100$  (107). Threshold cycle ( $C_{\text{T}}$ ) values equivalent to mock samples and non-template control were considered to be negative.

**Western blotting.** Whole cell lysates harvested in 2 $\times$  Laemmli buffer from time course infections were boiled at  $95^{\circ}\text{C}$  for 10 min. Proteins were separated by SDS-PAGE on 10% or 4 to 20% Mini-PROTEAN TGX Precast Protein Gels (Bio-Rad) according to the manufacturer's instructions. Proteins were transferred onto a 0.2  $\mu\text{m}$  Cytiva Amersham Protran Nitrocellulose membrane (Fisher Scientific) and blocked with 2% horse serum in 1 $\times$  Tris-buffered saline (20 mM Tris, 150 mM NaCl, pH 7.6) containing 0.01% Tween 20 detergent (Sigma-Aldrich) (TBS-T) for 1 h at room temperature. Membranes were then probed with primary antibodies diluted in 2% horse serum/TBS-T and incubated overnight at  $4^{\circ}\text{C}$  with agitation (Table 4). After three 5-min washes with TBS-T, membranes were incubated for 1 h at room temperature with secondary antibodies diluted in TBS-T (Table 4). Following three 5 min washes with TBS-T, membranes were imaged using an Odyssey XF imaging system (LI-COR). Analyses were performed with Image Studio Lite software (LI-COR).

**Virus purification and electrophoretic analysis of dsRNA and protein.** Virions were semipurified from SA11 and RF RV stocks using ultracentrifugation as described previously (103). Briefly, for RNA visualization, 50 mL of clarified RV stock was pelleted through a buffered 25% (wt/vol) sucrose cushion

(100 mM NaCl, 10 mM Tris-HCl [pH 7], 1 mM EDTA) using a SW32Ti rotor in a Beckman Coulter Optima Max-E ultracentrifuge at  $106,750 \times g$  for 90 min at 4°C. Viral pellets were resuspended in 350  $\mu$ L buffer RLT containing 3.5  $\mu$ L  $\beta$ -mercaptoethanol (Sigma-Aldrich) and dsRNA was extracted using an RNeasy minikit as described above. Purified RNA was treated with RNase A (Thermo Scientific) for 30 min at 37°C to specifically degrade single-stranded RNA and retain viral genomic dsRNA.

Extracted dsRNA was separated using 5% urea polyacrylamide gels in  $1 \times$  Tris-borate-EDTA (TBE) buffer (89 mM Tris-borate, 2 mM EDTA [pH 8.3]). Gels were fixed in gel fixing solution (30% [vol/vol] methanol in  $1 \times$  TBE buffer with 10% [vol/vol] acetic acid) and RNA was visualized using the Silver Stain Plus Kit (Bio-Rad) according to the manufacturer's instructions. Gels were dried onto filter paper and imaged using a Samsung Xpress C480FW scanner.

To visualize viral proteins of VP4 mutants, 25 mL of clarified RV stock was used for ultracentrifugation as described above. Viral pellets were resuspended in  $1 \times$  TNC buffer (20 mM Tris-HCl [pH 8], 100 mM NaCl, 1 mM  $\text{CaCl}_2$ ) and mixed 1:1 with  $2 \times$  Laemmli buffer followed by SDS-PAGE using 4 to 20% Mini-PROTEAN TGX Precast Protein Gels and staining with Coomassie brilliant blue R-250 (Bio-Rad) according to manufacturer's instructions. Gels were imaged using the Samsung Xpress C480FW scanner. Quantification was performed by densitometry of scanned gel images using Image J. Values were corrected for background noise and normalized to those of the WT virus.

**Indirect-binding ELISA.** To determine the antigenicity of viruses expressing SARS-CoV-2 peptides, 200  $\mu$ L of either viral supernatant (VP4 mutants) or cell lysate (NSP3 mutants) grown in the presence of trypsin (which cleaves VP4 into VP5\* and VP8\*, resulting in enhanced infectivity) (20) diluted in 0.1 M carbonate-bicarbonate buffer [pH 9.6] (Sigma-Aldrich) was immobilized on clear 96-well ELISA plates (Greiner Bio-One) and incubated overnight at 4°C with agitation. Following two washes with PBS containing 0.05% Tween 20 detergent (PBS-T) using a Biochrom Asys Atlantis microplate washer (Scientific Laboratory Supplies), plates were blocked with 2% horse serum/PBS at room temperature for 2 h. After blocking, plates were incubated with 100  $\mu$ L/well primary antibody (Table 4) diluted in 2% horse serum/PBS overnight at 4°C with agitation. Plates were then washed six times with PBS-T and incubated with horseradish peroxidase-conjugated goat anti-rabbit IgG (H+L) (1:2,000) (Bio-Rad) diluted in 2% horse serum/PBS for 1 h at room temperature with agitation. After 1 h, plates were washed three times with PBS-T and incubated with 2,2'-azino-bis(3-ethylbenzothiazoline-6-sulfonic acid) (Scientific Laboratory Supplies) substrate to allow the color to develop after which the reaction was terminated by adding 70  $\mu$ L per/well of 1% SDS solution. The optical density (OD) was measured at 405 nm using Cytation 3 Cell Imaging Multi-Mode Reader (Agilent) and data was analyzed using BioTek Gen5 software (Agilent). Three independent experiments were performed with standards done in triplicate. For a positive control, influenza A virus (IAV) strain A/Puerto Rico/8/1934 (PR8) was tagged with the same RBM sequence of the SARS-CoV-2 spike protein in the hemagglutinin (HA) protein (generated and validated in-house, unpublished data). The RBM sequence was inserted (by gene synthesis) between the C-terminal end of the HA signal peptide and the start of the head domain (between codons 17 and 18), placing the RBM sequence on the amino-terminus of the HA<sub>0</sub> molecule. This strategy was adapted from Li et al. (108), who successfully introduced large polypeptides (up to 140 amino acids) from *Bacillus anthracis* into IAV Aichi strain at this position. The synthetic constructs were cloned into a modified pHW2000 plasmid containing bidirectional RNA polymerase I and II promoters (109) and used for virus rescue as previously described (110, 111).

**Infection of bovine enteroids with NSP3 mutants.** 3D bovine enteroids were prepared as described in Hamilton et al. (112). Infection of organoids was carried out as described by Derricott et al. (70) and Blake et al. (113) with modifications. 3D organoids were mechanically disrupted into multicellular fragments by pipetting to expose the apical surface of the cells in 80% of the enteroids. The sheared enteroids were counted using a bright-field microscope and diluted to the final concentration of 2,500 enteroids/well. Each enteroid was estimated to contain approximately 40 cells as described by Blake et al. (113). The sheared enteroids were then diluted to the appropriate concentration with IntestiCult Organoid Growth Medium (STEMCELL Technologies) supplemented with 10  $\mu$ M ROCK pathway inhibitor (Cayman chemicals), 10  $\mu$ M Galunisertib (Cayman Chemicals), and 10  $\mu$ M p38 inhibitor (Enzo) and aliquoted into 15 mL falcon tubes for each condition. The enteroid fragment suspension was infected with NSP3 mutants at an approximate MOI of 10 and incubated for 1 h at 37°C. After 1 h, the enteroid/virus suspension was centrifuged at  $48 \times g$  for 2 min and washed five times by replacing the supernatant with equal volumes of fresh IntestiCult. Enteroid pellets were then resuspended in the appropriate volume of IntestiCult and 500  $\mu$ L plated onto Corning Matrigel (Scientific Laboratory Supplies) coated coverslips in a prewarmed 24-well plate.

**Immunofluorescent staining of bovine enteroids.** Enteroids were fixed at 1 and 24 hpi with 4% paraformaldehyde for 1.5 h at 4°C with agitation. Following three washes with PBS, enteroids were permeabilized with 0.5% Triton X-100 in PBS for 15 min and then blocked with 2% horse serum in PBS for 1 h, all at room temperature. Enteroids were incubated with primary antibodies (Table 4) overnight at 4°C with agitation and then washed three times with PBS and incubated with secondary antibodies (Table 4) and phalloidin (F-actin detection) (1:100) (Invitrogen) for 1 h at room temperature. All antibodies were diluted in 2% horse serum/PBS. Enteroids were then washed with PBS three times with the addition of 4',6-diamidino-2-phenylindole (DAPI) nuclear stain (1:5,000) (Invitrogen) for the final 10 min wash. Coverslips were rinsed in water, mounted onto microscope slides (Thermo Scientific) with ProLong Gold Antifade Mountant (Invitrogen) and imaged using a Zeiss LSM 710 confocal microscope at  $\times 630$  magnification. Images were analyzed using the Zen Black software and processed using Photoshop v23.1.1.

**Statistical analysis.** GraphPad Prism v9 was used for all statistical analyses. Data are presented as mean and standard deviation from three independent experiments with technical duplicates unless

otherwise stated. *P* values were determined by ratio paired *t* test and were considered statistically significant at  $<0.05$ , unless data were normalized in which case paired *t* tests were used.

## ACKNOWLEDGMENTS

We want to thank lab members, central support unit, bioimaging, and technical staff for their support and assistance with this project. We thank the MRC-Protein Phosphorylation and Ubiquitylation Unit, University of Dundee and Christine Tait-Burkard for providing SARS-CoV-2 spike antibodies and Marius Diebold for various software support.

This study was supported by an ISSF3 Award from the Wellcome Trust. J.S., P.D., and E.G. are supported by BBSRC Institute Strategic Program Grant funding (BB/P013740/1) from the British Biotechnology and Biological Sciences Research Council. O.D. is supported by a Roslin Studentship Award. R.B. is supported by the University of Edinburgh scholarship. S.C. is supported by a Wellcome Trust Clinical Research Career Development Fellowship (211138/Z/18/Z). A.B. and E.G. are Sir Henry Dale Fellows supported by the Wellcome Trust (213437/Z/18/Z and 211222\_Z\_18\_Z respectively). Funding for open access charge was from the Wellcome Trust.

We declare no conflicts of interest.

## REFERENCES

- Tate JE, Burton AH, Boschi-Pinto C, Parashar UD; World Health Organization–Coordinated Global Rotavirus Surveillance Network. 2016. Global, regional, and national estimates of rotavirus mortality in children  $<5$  years of age, 2000–2013. *Clin Infect Dis* 62(Suppl 2):S96–S105. <https://doi.org/10.1093/cid/civ1013>.
- Troeger C, Khalil IA, Rao PC, Cao S, Blacker BF, Ahmed T, Armah G, Bines JE, Brewer TG, Colombara DV, Kang G, Kirkpatrick BD, Kirkwood CD, Mwenda JM, Parashar UD, Petri WA, Riddle MS, Steele AD, Thompson RL, Walson JL, Sanders JW, Mokdad AH, Murray CJL, Hay SI, Reiner RC. 2018. Rotavirus vaccination and the global burden of rotavirus diarrhea among children younger than 5 years. *JAMA Pediatr* 172:958–965. <https://doi.org/10.1001/jamapediatrics.2018.1960>.
- Estes MK, G HB. 2013. *Rotaviruses*, p 1347–1401. In Knipe DM (ed), *Fields virology*. Wolters Kluwer Health/Lippincott Williams & Wilkins: Philadelphia, PA.
- Papp H, László B, Jakab F, Ganesh B, De Grazia S, Matthijnsens J, Ciarlet M, Martella V, Bányai K. 2013. Review of group A rotavirus strains reported in swine and cattle. *Vet Microbiol* 165:190–199. <https://doi.org/10.1016/j.vetmic.2013.03.020>.
- Urie NJ, Lombard JE, Shivley CB, Koprak CA, Adams AE, Earleywine TJ, Olson JD, Garry FB. 2018. Preweaned heifer management on US dairy operations: part V. factors associated with morbidity and mortality in preweaned dairy heifer calves. *J Dairy Sci* 101:9229–9244. <https://doi.org/10.3168/jds.2017-14019>.
- Windeyer MC, Leslie KE, Godden SM, Hodgins DC, Lissemore KD, LeBlanc SJ. 2014. Factors associated with morbidity, mortality, and growth of dairy heifer calves up to 3 months of age. *Prev Vet Med* 113:231–240. <https://doi.org/10.1016/j.prevetmed.2013.10.019>.
- Kim H-J, Park J, Matthijnsens J, Lee JH, Bae YC, Alfajaro MM, Park SI, Kang MI, Cho KO. 2011. Intestinal and extra-intestinal pathogenicity of a bovine reassortant rotavirus in calves and piglets. *Vet Microbiol* 152:291–303. <https://doi.org/10.1016/j.vetmic.2011.05.017>.
- Bergman H, Henschke N, Hungerford D, Pitan F, Ndwandwe D, Cunliffe N, Soares-Weiser K. 2021. Vaccines for preventing rotavirus diarrhoea: vaccines in use. *Cochrane Database Syst Rev* 11:CD008521. <https://doi.org/10.1002/14651858.CD008521.pub6>.
- Ciarlet M, Schödel F. 2009. Development of a rotavirus vaccine: clinical safety, immunogenicity, and efficacy of the pentavalent rotavirus vaccine, RotaTeq. *Vaccine* 27(Suppl 6):G72–G81. <https://doi.org/10.1016/j.vaccine.2009.09.107>.
- Burnett E, Jonesteller CL, Tate JE, Yen C, Parashar UD. 2017. Global impact of rotavirus vaccination on childhood hospitalizations and mortality from diarrhea. *J Infect Dis* 215:1666–1672. <https://doi.org/10.1093/infdis/jix186>.
- Meganck V, Hoflack G, Piepers S, Opsomer G. 2015. Evaluation of a protocol to reduce the incidence of neonatal calf diarrhoea on dairy herds. *Prev Vet Med* 118:64–70. <https://doi.org/10.1016/j.prevetmed.2014.11.007>.
- Viidu D-A, Mõtus K. 2022. Implementation of a pre-calving vaccination programme against rotavirus, coronavirus and enterotoxigenic *Escherichia coli* (F5) and association with dairy calf survival. *BMC Vet Res* 18:59. <https://doi.org/10.1186/s12917-022-03154-2>.
- Saif LJ, Fernandez FM. 1996. Group A rotavirus veterinary vaccines. *J Infect Dis* 174:S98–S106. [https://doi.org/10.1093/infdis/174.Supplement\\_1.S98](https://doi.org/10.1093/infdis/174.Supplement_1.S98).
- Chattha KS, Roth JA, Saif LJ. 2015. Strategies for design and application of enteric viral vaccines. *Annu Rev Anim Biosci* 3:375–395. <https://doi.org/10.1146/annurev-animal-022114-111038>.
- Rainsford EW, McCrae MA. 2007. Characterization of the NSP6 protein product of rotavirus gene 11. *Virus Res* 130:193–201. <https://doi.org/10.1016/j.virusres.2007.06.011>.
- Mattion NM, Mitchell DB, Both GW, Estes MK. 1991. Expression of rotavirus proteins encoded by alternative open reading frames of genome segment 11. *Virology* 181:295–304. [https://doi.org/10.1016/0042-6822\(91\)90495-W](https://doi.org/10.1016/0042-6822(91)90495-W).
- Crawford SE, Ramani S, Tate JE, Parashar UD, Svensson L, Hagbom M, Franco MA, Greenberg HB, O’Ryan M, Kang G, Desselberger U, Estes MK. 2017. Rotavirus infection. *Nat Rev Dis Primers* 3:17083. <https://doi.org/10.1038/nrdp.2017.83>.
- Amimo JO, Raev SA, Chepngeno J, Mainga AO, Guo Y, Saif L, Vlasova AN. 2021. Rotavirus interactions with host intestinal epithelial cells. *Front Immunol* 12:793841. <https://doi.org/10.3389/fimmu.2021.793841>.
- Dormitzer PR, Nason EB, Prasad BVV, Harrison SC. 2004. Structural rearrangements in the membrane penetration protein of a non-enveloped virus. *Nature* 430:1053–1058. <https://doi.org/10.1038/nature02836>.
- Crawford SE, Mukherjee SK, Estes MK, Lawton JA, Shaw AL, Ramig RF, Prasad BV. 2001. Trypsin cleavage stabilizes the rotavirus VP4 spike. *J Virol* 75:6052–6061. <https://doi.org/10.1128/JVI.75.13.6052-6061.2001>.
- Arias CF, Romero P, Alvarez V, López S. 1996. Trypsin activation pathway of rotavirus infectivity. *J Virol* 70:5832–5839. <https://doi.org/10.1128/jvi.70.9.5832-5839.1996>.
- Estes MK, Graham DY, Mason BB. 1981. Proteolytic enhancement of rotavirus infectivity: molecular mechanisms. *J Virol* 39:879–888. <https://doi.org/10.1128/jvi.39.3.879-888.1981>.
- Hu L, Crawford SE, Czako R, Cortes-Penfield NW, Smith DF, Le Pendu J, Estes MK, Prasad BVV. 2012. Cell attachment protein VP8\* of a human rotavirus specifically interacts with A-type histo-blood group antigen. *Nature* 485:256–259. <https://doi.org/10.1038/nature10996>.
- Sun X, Li D, Duan Z. 2021. Structural basis of glycan recognition of rotavirus. *Front Mol Biosci* 8:658029. <https://doi.org/10.3389/fmolb.2021.658029>.
- Fiore L, Greenberg HB, Mackow ER. 1991. The VP8 fragment of VP4 is the rhesus rotavirus hemagglutinin. *Virology* 181:553–563. [https://doi.org/10.1016/0042-6822\(91\)90888-1](https://doi.org/10.1016/0042-6822(91)90888-1).
- Patton JT. 1996. Rotavirus VP1 alone specifically binds to the 3’ end of viral mRNA, but the interaction is not sufficient to initiate minus-strand synthesis. *J Virol* 70:7940–7947. <https://doi.org/10.1128/jvi.70.11.7940-7947.1996>.

27. Trask SD, McDonald SM, Patton JT. 2012. Structural insights into the coupling of virion assembly and rotavirus replication. *Nat Rev Microbiol* 10:165–177. <https://doi.org/10.1038/nrmicro2673>.
28. Lu X, McDonald SM, Tortorici MA, Tao YJ, Vasquez-Del Carpio R, Nibert ML, Patton JT, Harrison SC. 2008. Mechanism for coordinated RNA packaging and genome replication by rotavirus polymerase VP1. *Structure* 16:1678–1688. <https://doi.org/10.1016/j.str.2008.09.006>.
29. Borodavka A, Desselberger U, Patton JT. 2018. Genome packaging in multi-segmented dsRNA viruses: distinct mechanisms with similar outcomes. *Curr Opin Virol* 33:106–112. <https://doi.org/10.1016/j.coviro.2018.08.001>.
30. Ding K, Celma CC, Zhang X, Chang T, Shen W, Atanasov I, Roy P, Zhou ZH. 2019. In situ structures of rotavirus polymerase in action and mechanism of mRNA transcription and release. *Nat Commun* 10:2216. <https://doi.org/10.1038/s41467-019-10236-7>.
31. Chizhikov V, Patton JT. 2000. A four-nucleotide translation enhancer in the 3'-terminal consensus sequence of the nonpolyadenylated mRNAs of rotavirus. *RNA* 6:814–825. <https://doi.org/10.1017/S1355838200992264>.
32. Piron M, Delaunay T, Grosclaude J, Poncet D. 1999. Identification of the RNA-binding, dimerization, and eIF4GI-binding domains of rotavirus nonstructural protein NSP3. *J Virol* 73:5411–5421. <https://doi.org/10.1128/JVI.73.7.5411-5421.1999>.
33. Piron M, Vende P, Cohen J, Poncet D. 1998. Rotavirus RNA-binding protein NSP3 interacts with eIF4GI and evicts the poly(A) binding protein from eIF4F. *EMBO J* 17:5811–5821. <https://doi.org/10.1093/emboj/17.19.5811>.
34. Harb M, Becker MM, Vitour D, Baron CH, Vende P, Brown SC, Bolte S, Arold ST, Poncet D. 2008. Nuclear localization of cytoplasmic poly(A)-binding protein upon rotavirus infection involves the interaction of NSP3 with eIF4G and RoXan. *J Virol* 82:11283–11293. <https://doi.org/10.1128/JVI.00872-08>.
35. Rubio RM, Mora SI, Romero P, Arias CF, López S. 2013. Rotavirus prevents the expression of host responses by blocking the nucleocytoplasmic transport of polyadenylated mRNAs. *J Virol* 87:6336–6345. <https://doi.org/10.1128/JVI.00361-13>.
36. Padilla-Noriega L, Paniagua O, Guzmán-León S. 2002. Rotavirus protein NSP3 shuts off host cell protein synthesis. *Virology* 298:1–7. <https://doi.org/10.1006/viro.2002.1477>.
37. Montero H, Arias CF, Lopez S. 2006. Rotavirus nonstructural protein NSP3 is not required for viral protein synthesis. *J Virol* 80:9031–9038. <https://doi.org/10.1128/JVI.00437-06>.
38. Komoto S, Sasaki J, Taniguchi K. 2006. Reverse genetics system for introduction of site-specific mutations into the double-stranded RNA genome of infectious rotavirus. *Proc Natl Acad Sci U S A* 103:4646–4651. <https://doi.org/10.1073/pnas.0509385103>.
39. Trask SD, Taraporewala ZF, Boehme KW, Dermody TS, Patton JT. 2010. Dual selection mechanisms drive efficient single-gene reverse genetics for rotavirus. *Proc Natl Acad Sci U S A* 107:18652–18657. <https://doi.org/10.1073/pnas.1011948107>.
40. Troupin C, Dehée A, Schnuriger A, Vende P, Poncet D, Garbarg-Chenon A. 2010. Rearranged genomic RNA segments offer a new approach to the reverse genetics of rotaviruses. *J Virol* 84:6711–6719. <https://doi.org/10.1128/JVI.00547-10>.
41. John R, Reetz J, Kauffer BB, Trojnar E. 2016. Generation of an avian-mammalian rotavirus reassortant by using a helper virus-dependent reverse genetics system. *J Virol* 90:1439–1443. <https://doi.org/10.1128/JVI.02730-15>.
42. Kanai Y, Komoto S, Kawagishi T, Nouda R, Nagasawa N, Onishi M, Matsuura Y, Taniguchi K, Kobayashi T. 2017. Entirely plasmid-based reverse genetics system for rotaviruses. *Proc Natl Acad Sci U S A* 114:2349–2354. <https://doi.org/10.1073/pnas.1618424114>.
43. Komoto S, Fukuda S, Ide T, Ito N, Sugiyama M, Yoshikawa T, Murata T, Taniguchi K. 2018. Generation of recombinant rotaviruses expressing fluorescent proteins by using an optimized reverse genetics system. *J Virol* 92:e00588-18. <https://doi.org/10.1128/JVI.00588-18>.
44. Sánchez-Tacuba L, Feng N, Meade NJ, Mellits KH, Jais PH, Yasukawa LL, Resch TK, Jiang B, López S, Ding S, Greenberg HB. 2020. An optimized reverse genetics system suitable for efficient recovery of simian, human, and murine-like rotaviruses. *J Virol* 94:e01294-20. <https://doi.org/10.1128/JVI.01294-20>.
45. Philip AA, Perry JL, Eaton HE, Shmulevitz M, Hyser JM, Patton JT. 2019. Generation of recombinant rotavirus expressing NSP3-UnaG fusion protein by a simplified reverse genetics system. *J Virol* 93:e01616-19. <https://doi.org/10.1128/JVI.01616-19>.
46. Kanai Y, Onishi M, Kawagishi T, Pannacha P, Nurdin JA, Nouda R, Yamasaki M, Lusiany T, Khamrin P, Okitsu S, Hayakawa S, Ebina H, Ushijima H, Kobayashi T. 2020. Reverse genetics approach for developing rotavirus vaccine candidates carrying VP4 and VP7 genes cloned from clinical isolates of human rotavirus. *J Virol* 95:e01374-20. <https://doi.org/10.1128/JVI.01374-20>.
47. Falkenhagen A, Huyzers M, van Dijk AA, John R. 2021. Rescue of infectious rotavirus reassortants by a reverse genetics system is restricted by the receptor-binding region of VP4. *Viruses* 13:363. <https://doi.org/10.3390/v13030363>.
48. Uprety T, Wang D, Li F. 2021. Recent advances in rotavirus reverse genetics and its utilization in basic research and vaccine development. *Arch Virol* 166:2369–2386. <https://doi.org/10.1007/s00705-021-05142-7>.
49. Nair N, Feng N, Blum LK, Sanyal M, Ding S, Jiang B, Sen A, Morton JM, He X-S, Robinson WH, Greenberg HB. 2017. VP4- and VP7-specific antibodies mediate heterotypic immunity to rotavirus in humans. *Sci Transl Med* 9:e005434. <https://doi.org/10.1126/scitranslmed.aam5434>.
50. Feng N, Hu L, Ding S, Sanyal M, Zhao B, Sankaran B, Ramani S, McNeal M, Yasukawa LL, Song Y, Prasad BVV, Greenberg HB. 2019. Human VP8\* mAbs neutralize rotavirus selectively in human intestinal epithelial cells. *J Clin Invest* 129:3839–3851. <https://doi.org/10.1172/JCI128382>.
51. Philip AA, Patton JT. 2020. Expression of separate heterologous proteins from the rotavirus nsp3 genome segment using a translational 2A stop-restart element. *J Virol* 94:e00959-20. <https://doi.org/10.1128/JVI.00959-20>.
52. Philip AA, Patton JT. 2021. Rotavirus as an expression platform of domains of the SARS-CoV-2 spike protein. *Vaccines (Basel)* 9:449. <https://doi.org/10.3390/vaccines9050449>.
53. Krammer F. 2020. SARS-CoV-2 vaccines in development. *Nature* 586:516–527. <https://doi.org/10.1038/s41586-020-2798-3>.
54. Kyriakidis NC, López-Cortés A, González EV, Grimaldos AB, Prado EO. 2021. SARS-CoV-2 vaccines strategies: a comprehensive review of phase 3 candidates. *NPJ Vaccines* 6:28. <https://doi.org/10.1038/s41541-021-00292-w>.
55. Hassan AO, Kafai NM, Dmitriev IP, Fox JM, Smith BK, Harvey IB, Chen RE, Winkler ES, Wessel AW, Case JB, Kashentseva E, McCune BT, Bailey AL, Zhao H, VanBlargan LA, Dai Y-N, Ma M, Adams LJ, Shrihari S, Danis JE, Gralinski LE, Hou YJ, Schäfer A, Kim AS, Keeler SP, Weiskopf D, Baric RS, Holtzman MJ, Fremont DH, Curtiel DT, Diamond MS. 2020. A single-dose intranasal ChAd vaccine protects upper and lower respiratory tracts against SARS-CoV-2. *Cell* 183:169–184.e13. <https://doi.org/10.1016/j.cell.2020.08.026>.
56. Bos R, Rutten L, van der Lubbe JEM, Bakkers MJG, Hardenberg G, Wegmann F, Zuijdgheest D, de Wilde AH, Koornneef A, Verwilligen A, van Manen D, Kwaks T, Vogels R, Dalebout TJ, Myeni SK, Kikkert M, Snijder EJ, Li Z, Barouch DH, Vellinga J, Langedijk JPM, Zahn RC, Custers J, Schuitemaker H. 2020. Ad26 vector-based COVID-19 vaccine encoding a prefusion-stabilized SARS-CoV-2 Spike immunogen induces potent humoral and cellular immune responses. *NPJ Vaccines* 5: 91–91. <https://doi.org/10.1038/s41541-020-00243-x>.
57. Sahin U, Muik A, Derhovanessian E, Vogler I, Kranz LM, Vormehr M, Baum A, Pascal K, Quandt J, Maurus D, Brachtendorf S, Lörks V, Sikorski J, Hilker R, Becker D, Eller A-K, Grützner J, Boesler C, Rosenbaum C, Kühnle M-C, Luxemburger U, Kemmer-Brück A, Langer D, Bexon M, Bolte S, Karikó K, Palanche T, Fischer B, Schultz A, Shi P-Y, Fontes-Garfias C, Perez JL, Swanson KA, Loschko J, Scully IL, Cutler M, Kalina W, Kyrtasous CA, Cooper D, Dormitzer PR, Jansen KU, Türeci Ö. 2020. COVID-19 vaccine BNT162b1 elicits human antibody and TH1 T cell responses. *Nature* 586:594–599. <https://doi.org/10.1038/s41586-020-2814-7>.
58. Wang Z, Schmidt F, Weisblum Y, Muecksch F, Barnes CO, Finkina S, Schaefer-Babajew D, Cipolla M, Gaebler C, Lieberman JA, Oliveira TY, Yang Z, Abernathy ME, Huey-Tubman KE, Hurley A, Turroja M, West KA, Gordon K, Millard KG, Ramos V, Da Silva J, Xu J, Colbert RA, Patel R, Dizon J, Unson-O'Brien C, Shimeliovich I, Gazumyan A, Caskey M, Bjorkman PJ, Casellas R, Hatzioannou T, Bieniasz PD, Nussenzweig MC. 2021. mRNA vaccine-elicited antibodies to SARS-CoV-2 and circulating variants. *Nature* 592:616–622. <https://doi.org/10.1038/s41586-021-03324-6>.
59. Yang J, Wang W, Chen Z, Lu S, Yang F, Bi Z, Bao L, Mo F, Li X, Huang Y, Hong W, Yang Y, Zhao Y, Ye F, Lin S, Deng W, Chen H, Lei H, Zhang Z, Luo M, Gao H, Zheng Y, Gong Y, Jiang X, Xu Y, Lv Q, Li D, Wang M, Li F, Wang S, Wang G, Yu P, Qu Y, Yang L, Deng H, Tong A, Li J, Wang Z, Yang J, Shen G, Zhao Z, Li Y, Luo J, Liu H, Yu W, Yang M, Xu J, Wang J, Li H, Wang H, et al. 2020. A vaccine targeting the RBD of the S protein of SARS-CoV-2 induces protective immunity. *Nature* 586:572–577. <https://doi.org/10.1038/s41586-020-2599-8>.

60. Liu Z, Xu W, Xia S, Gu C, Wang X, Wang Q, Zhou J, Wu Y, Cai X, Qu D, Ying T, Xie Y, Lu L, Yuan Z, Jiang S. 2020. RBD-Fc-based COVID-19 vaccine candidate induces highly potent SARS-CoV-2 neutralizing antibody response. *Signal Transduct Target Ther* 5:282. <https://doi.org/10.1038/s41392-020-00402-5>.
61. Piccoli L, Park Y-J, Tortorici MA, Czudnochowski N, Walls AC, Beltramello M, Silacci-Fregni C, Pinto D, Rosen LE, Bowen JE, Acton OJ, Jaconi S, Guarino B, Minola A, Zatta F, Sprugasci N, Bassi J, Peter A, De Marco A, Nix JC, Mele F, Jovic S, Rodriguez BF, Gupta SV, Jin F, Piumatti G, Lo Presti G, Pellanda AF, Biggiogero M, Tarkowski M, Pizzuto MS, Cameroni E, Havenar-Daughton C, Smithey M, Hong D, Lepori V, Albanese E, Ceschi A, Bernasconi E, Elzi L, Ferrari P, Garzoni C, Riva A, Snell G, Sallusto F, Fink K, Virgin HW, Lanzavecchia A, Corti D, Velesler D. 2020. Mapping neutralizing and immunodominant sites on the SARS-CoV-2 spike receptor-binding domain by structure-guided high-resolution serology. *Cell* 183:1024–1042.e21. <https://doi.org/10.1016/j.cell.2020.09.037>.
62. Lan J, Ge J, Yu J, Shan S, Zhou H, Fan S, Zhang Q, Shi X, Wang Q, Zhang L, Wang X. 2020. Structure of the SARS-CoV-2 spike receptor-binding domain bound to the ACE2 receptor. *Nature* 581:215–220. <https://doi.org/10.1038/s41586-020-2180-5>.
63. Settembre EC, Chen JZ, Dormitzer PR, Grigorieff N, Harrison SC. 2011. Atomic model of an infectious rotavirus particle. *EMBO J* 30:408–416. <https://doi.org/10.1038/emboj.2010.322>.
64. Herrmann T, Torres R, Salgado EN, Berciu C, Stoddard D, Nicastro D, Jenni S, Harrison SC. 2021. Functional refolding of the penetration protein on a non-enveloped virus. *Nature* 590:666–670. <https://doi.org/10.1038/s41586-020-03124-4>.
65. Rodríguez JM, Chichón FJ, Martín-Forero E, González-Camacho F, Carrascosa JL, Castón JR, Luque D. 2014. New insights into rotavirus entry machinery: stabilization of rotavirus spike conformation is independent of trypsin cleavage. *PLoS Pathog* 10:e1004157. <https://doi.org/10.1371/journal.ppat.1004157>.
66. Liu Z, Chen O, Wall JBJ, Zheng M, Zhou Y, Wang L, Vaseghi HR, Qian L, Liu J. 2017. Systematic comparison of 2A peptides for cloning multi-genes in a polycistronic vector. *Sci Rep* 7:2193. <https://doi.org/10.1038/s41598-017-02460-2>.
67. Borodavka A, Dykeman EC, Schrimpf W, Lamb DC. 2017. Protein-mediated RNA folding governs sequence-specific interactions between rotavirus genome segments. *Elife* 6:e27453. <https://doi.org/10.7554/eLife.27453>.
68. McDonald SM, Patton JT. 2011. Assortment and packaging of the segmented rotavirus genome. *Trends Microbiol* 19:136–144. <https://doi.org/10.1016/j.tim.2010.12.002>.
69. Bravo JPK, Bartnik K, Venditti L, Acker J, Gail EH, Colyer A, Davidovich C, Lamb DC, Tuma R, Calabrese AN, Borodavka A. 2021. Structural basis of rotavirus RNA chaperone displacement and RNA annealing. *Proc Natl Acad Sci U S A* 118:e2100198118. <https://doi.org/10.1073/pnas.2100198118>.
70. Derricott H, Luu L, Fong WY, Hartley CS, Johnston LJ, Armstrong SD, Randle N, Duckworth CA, Campbell BJ, Wastling JM, Coombes JL. 2019. Developing a 3D intestinal epithelium model for livestock species. *Cell Tissue Res* 375:409–424. <https://doi.org/10.1007/s00441-018-2924-9>.
71. L'Haridon R, Scherrer R. 1976. [In vitro culture of a rotavirus associated with neonatal calf diarrhoea] *Ann Rech Vet* 7:373–381.
72. Papa G, Borodavka A, Desselberger U. 2021. Viroplasm: assembly and functions of rotavirus replication factories. *Viruses* 13:1349. <https://doi.org/10.3390/v13071349>.
73. Wen X, Cao D, Jones RW, Li J, Szu S, Hoshino Y. 2012. Construction and characterization of human rotavirus recombinant VP8\* subunit parenteral vaccine candidates. *Vaccine* 30:6121–6126. <https://doi.org/10.1016/j.vaccine.2012.07.078>.
74. Park W-J, Yoon Y-K, Park J-S, Pansuriya R, Seok Y-J, Ganapathy R. 2021. Rotavirus spike protein ΔVP8\* as a novel carrier protein for conjugate vaccine platform with demonstrated antigenic potential for use as bivalent vaccine. *Sci Rep* 11:22037. <https://doi.org/10.1038/s41598-021-01549-z>.
75. Xia M, Huang P, Jiang X, Tan M. 2021. A nanoparticle-based trivalent vaccine targeting the glycan binding VP8\* domains of rotaviruses. *Viruses* 13:72. <https://doi.org/10.3390/v13010072>.
76. Tan M, Huang P, Xia M, Fang P-A, Zhong W, McNeal M, Wei C, Jiang W, Jiang X. 2011. Norovirus P particle, a novel platform for vaccine development and antibody production. *J Virol* 85:753–764. <https://doi.org/10.1128/JVI.01835-10>.
77. Wen X, Cao D, Jones RW, Hoshino Y, Yuan L. 2015. Tandem truncated rotavirus VP8\* subunit protein with T cell epitope as non-replicating parenteral vaccine is highly immunogenic. *Hum Vaccin Immunother* 11:2483–2489. <https://doi.org/10.1080/21645515.2015.1054583>.
78. Li Y, Xue M, Yu L, Luo G, Yang H, Jia L, Zeng Y, Li T, Ge S, Xia N. 2018. Expression and characterization of a novel truncated rotavirus VP4 for the development of a recombinant rotavirus vaccine. *Vaccine* 36:2086–2092. <https://doi.org/10.1016/j.vaccine.2018.03.011>.
79. Komoto S, Kugita M, Sasaki J, Taniguchi K. 2008. Generation of recombinant rotavirus with an antigenic mosaic of cross-reactive neutralization epitopes on VP4. *J Virol* 82:6753–6757. <https://doi.org/10.1128/JVI.00601-08>.
80. Harrison SC. 2008. Viral membrane fusion. *Nat Struct Mol Biol* 15:690–698. <https://doi.org/10.1038/nsmb.1456>.
81. Trask SD, Kim IS, Harrison SC, Dormitzer PR. 2010. A rotavirus spike protein conformational intermediate binds lipid bilayers. *J Virol* 84:1764–1770. <https://doi.org/10.1128/JVI.01682-09>.
82. Dormitzer PR, Greenberg HB, Harrison SC. 2001. Proteolysis of monomeric recombinant rotavirus VP4 yields an oligomeric VP5\* core. *J Virol* 75:7339–7350. <https://doi.org/10.1128/JVI.75.16.7339-7350.2001>.
83. Kim IS, Trask SD, Babyonyshev M, Dormitzer PR, Harrison SC. 2010. Effect of mutations in VP5 hydrophobic loops on rotavirus cell entry. *J Virol* 84:6200–6207. <https://doi.org/10.1128/JVI.02461-09>.
84. Yoder JD, Trask SD, Vo TP, Binka M, Feng N, Harrison SC, Greenberg HB, Dormitzer PR. 2009. VP5\* rearranges when rotavirus uncoats. *J Virol* 83:11372–11377. <https://doi.org/10.1128/JVI.01228-09>.
85. Trask SD, Dormitzer PR. 2006. Assembly of highly infectious rotavirus particles re-coated with recombinant outer capsid proteins. *J Virol* 80:11293–11304. <https://doi.org/10.1128/JVI.01346-06>.
86. Caddy SL, Vaysburd M, Wing M, Foss S, Andersen JT, O'Connell K, Mayes K, Higginson K, Iturriza-Gómara M, Desselberger U, James LC. 2020. Intracellular neutralisation of rotavirus by VP6-specific IgG. *PLoS Pathog* 16:e1008732. <https://doi.org/10.1371/journal.ppat.1008732>.
87. Vesikari T, Matson DO, Dennehy P, Van Damme P, Santosham M, Rodriguez Z, Dallas MJ, Heyse JF, Goveia MG, Black SB, Shinefield HR, Christie CDC, Ylitalo S, Itzler RF, Coia ML, Onorato MT, Adeyi BA, Marshall GS, Gothefer L, Campens D, Karvonen A, Watt JP, O'Brien KL, DiNubile MJ, Clark HF, Boslego JW, Offit PA, Heaton PM, Rotavirus Efficacy and Safety Trial (REST) Study Team. 2006. Safety and efficacy of a pentavalent human-bovine (WC3) reassortant rotavirus vaccine. *N Engl J Med* 354:23–33. <https://doi.org/10.1056/NEJMoa052664>.
88. Angel J, Franco MA, Greenberg HB. 2007. Rotavirus vaccines: recent developments and future considerations. *Nat Rev Microbiol* 5:529–539. <https://doi.org/10.1038/nrmicro1692>.
89. Bernstein DI, Smith VE, Sherwood JR, Schiff GM, Sander DS, DeFeudis D, Spriggs DR, Ward RL. 1998. Safety and immunogenicity of live, attenuated human rotavirus vaccine 89-12. *Vaccine* 16:381–387. [https://doi.org/10.1016/S0264-410X\(97\)00210-7](https://doi.org/10.1016/S0264-410X(97)00210-7).
90. Bernstein DI, Sack DA, Rothstein E, Reisinger K, Smith VE, O'Sullivan D, Spriggs DR, Ward RL. 1999. Efficacy of live, attenuated, human rotavirus vaccine 89-12 in infants: a randomised placebo-controlled trial. *Lancet* 354:287–290. [https://doi.org/10.1016/S0140-6736\(98\)12106-2](https://doi.org/10.1016/S0140-6736(98)12106-2).
91. Gratia M, Vende P, Charpilienne A, Baron HC, Laroche C, Sarot E, Pyronnet S, Duarte M, Poncet D. 2016. Challenging the roles of NSP3 and untranslated regions in rotavirus mRNA translation. *PLoS One* 11:e0145998. <https://doi.org/10.1371/journal.pone.0145998>.
92. Jang YH, Seong BL. 2012. Principles underlying rational design of live attenuated influenza vaccines. *Clin Exp Vaccine Res* 1:35–49. <https://doi.org/10.7774/cevr.2012.1.1.35>.
93. Desselberger U. 2020. What are the limits of the packaging capacity for genomic RNA in the cores of rotaviruses and of other members of the Reoviridae? *Virus Res* 276:197822. <https://doi.org/10.1016/j.virusres.2019.197822>.
94. Buchholz UJ, Finke S, Conzelmann K-K. 1999. Generation of bovine respiratory syncytial virus (BRSV) from cDNA: BRSV NS2 is not essential for virus replication in tissue culture, and the human RSV leader region acts as a functional BRSV genome promoter. *J Virol* 73:251–259. <https://doi.org/10.1128/JVI.73.1.251-259.1999>.
95. Taniguchi K, Nishikawa K, Kobayashi N, Urasawa T, Wu H, Gorziglia M, Urasawa S. 1994. Differences in plaque size and VP4 sequence found in SA11 virus clones having simian authentic VP4. *Virology* 198:325–330. <https://doi.org/10.1006/viro.1994.1035>.
96. Richards JE, Desselberger U, Lever AM. 2013. Experimental pathways towards developing a rotavirus reverse genetics system: synthetic full length rotavirus ssRNAs are neither infectious nor translated in permissive cells. *PLoS One* 8:e74328. <https://doi.org/10.1371/journal.pone.0074328>.
97. Dormitzer PR, Sun Z-Y, Wagner G, Harrison SC. 2002. The rhesus rotavirus VP4 sialic acid binding domain has a galectin fold with a novel carbohydrate binding site. *EMBO J* 21:885–897. <https://doi.org/10.1093/emboj/21.5.885>.

98. Yi Z, Ling Y, Zhang X, Chen J, Hu K, Wang Y, Song W, Ying T, Zhang R, Lu H, Yuan Z. 2020. Functional mapping of B-cell linear epitopes of SARS-CoV-2 in COVID-19 convalescent population. *Emerg Microbes Infect* 9: 1988–1996. <https://doi.org/10.1080/22221751.2020.1815591>.
99. Polyiam K, Phoolcharoen W, Butkhot N, Srisaowakarn C, Thitithanyanont A, Auewarakul P, Hoonswuan T, Ruengjitchatchawalya M, Mekvichitsaeng P, Roshorm YM. 2021. Immunodominant linear B cell epitopes in the spike and membrane proteins of SARS-CoV-2 identified by immunoinformatics prediction and immunoassay. *Sci Rep* 11:20383. <https://doi.org/10.1038/s41598-021-99642-w>.
100. Daniels RW, Rossano AJ, Macleod GT, Ganetzky B. 2014. Expression of multiple transgenes from a single construct using viral 2A peptides in *Drosophila*. *PLoS One* 9:e100637. <https://doi.org/10.1371/journal.pone.0100637>.
101. Jeong YS, Ku H-K, Jung Y-J, Kim JK, Lee KB, Kim J-K, Lim S-H, Lee D, Ha S-H. 2021. 2A-linked bi-, tri-, and quad-cistrons for the stepwise biosynthesis of  $\beta$ -carotene, zeaxanthin, and ketocarotenoids in rice endosperm. *Metab Eng Commun* 12:e00166. <https://doi.org/10.1016/j.mec.2021.e00166>.
102. Simmonds P. 2012. SSE: a nucleotide and amino acid sequence analysis platform. *BMC Res Notes* 5:50. <https://doi.org/10.1186/1756-0500-5-50>.
103. Arnold M, Patton JT, McDonald SM. 2009. Culturing, storage, and quantification of rotaviruses. *Curr Protoc Microbiol* 15:Unit-15C.3. <https://doi.org/10.1002/9780471729259.mc15c03s15>.
104. Matrosovich M, Matrosovich T, Garten W, Klenk H-D. 2006. New low-viscosity overlay medium for viral plaque assays. *Virology* 343:63–66. <https://doi.org/10.1016/j.virusres.2004.02.028>.
105. Kibbe WA. 2007. OligoCalc: an online oligonucleotide properties calculator. *Nucleic Acids Res* 35:W43–W46. <https://doi.org/10.1093/nar/gkm234>.
106. Schmittgen TD, Livak KJ. 2008. Analyzing real-time PCR data by the comparative CT method. *Nat Protoc* 3:1101–1108. <https://doi.org/10.1038/nprot.2008.73>.
107. Mygind T, Birkelund S, Birkebaek NH, Østergaard L, Jensen JS, Christiansen G. 2002. Determination of PCR efficiency in chelex-100 purified clinical samples and comparison of real-time quantitative PCR and conventional PCR for detection of *Chlamydia pneumoniae*. *BMC Microbiol* 2:17. <https://doi.org/10.1186/1471-2180-2-17>.
108. Li Z-N, Mueller SN, Ye L, Bu Z, Yang C, Ahmed R, Steinhauer DA. 2005. Chimeric influenza virus hemagglutinin proteins containing large domains of the *Bacillus anthracis* protective antigen: protein characterization, incorporation into infectious influenza viruses, and antigenicity. *J Virol* 79: 10003–10012. <https://doi.org/10.1128/JVI.79.15.10003-10012.2005>.
109. de Wit E, Spronken MIJ, Bestebroer TM, Rimmelzwaan GF, Osterhaus ADME, Fouchier RAM. 2004. Efficient generation and growth of influenza virus A/PR/8/34 from eight cDNA fragments. *Virus Res* 103:155–161. <https://doi.org/10.1016/j.virusres.2004.02.028>.
110. Hutchinson EC, Curran MD, Read EK, Gog JR, Digard P. 2008. Mutational analysis of cis-acting RNA signals in segment 7 of influenza A virus. *J Virol* 82:11869–11879. <https://doi.org/10.1128/JVI.01634-08>.
111. Wise HM, Foeglein A, Sun J, Dalton RM, Patel S, Howard W, Anderson EC, Barclay WS, Digard P. 2009. A complicated message: Identification of a novel PB1-related protein translated from influenza A virus segment 2 mRNA. *J Virol* 83:8021–8031. <https://doi.org/10.1128/JVI.00826-09>.
112. Hamilton CA, Young R, Jayaraman S, Sehgal A, Paxton E, Thomson S, Katzer F, Hope J, Innes E, Morrison LJ, Mabbott NA. 2018. Development of in vitro enteroids derived from bovine small intestinal crypts. *Vet Res* 49:54. <https://doi.org/10.1186/s13567-018-0547-5>.
113. Blake R, Jensen K, Mabbott N, Hope J, Stevens J. 2022. Development of 3D bovine intestinal organoid derived models to investigate *Mycobacterium avium* ssp *paratuberculosis* pathogenesis. *bioRxiv*. <https://www.biorxiv.org/content/10.1101/2022.05.13.491821v1>.